PCCP

ROYAL SOCIETY OF CHEMISTRY

PAPER

View Article Online
View Journal | View Issue

Cite this: *Phys. Chem. Chem. Phys.*, 2023, **25**, 21020

The E_3 state of FeMoco: one hydride, two hydrides or dihydrogen?†

Yunjie Pang[ab] and Ragnar Bjornsson *[bc]

Hydrides are present in the reduced states of the iron-molybdenum cofactor (FeMoco) of Mo nitrogenase and are believed to play a key mechanistic role in the dinitrogen reduction reaction catalyzed by the enzyme. Two hydrides are present in the **E_4** state according to ^{1}H ENDOR and there is likely a single hydride in the **E_2** redox state. The 2-hydride **E_4** state has been experimentally observed to bind N_2 and it has been speculated that **E_3** may bind N_2 as well. However, the **E_3** state has not been directly observed and very little is known about its molecular and electronic structure or reactivity. In recent computational studies, we have explored the energy surfaces of the **E_2** and **E_4** by QM/MM modelling, and found that the most stable hydride isomers contain bridging or partially bridging hydrides with an open protonated belt sulfide-bridge. In this work we systematically explore the energy surface of the **E_3** redox state, comparing single hydride and two-hydride isomers with varying coordination and bridging *vs.* terminal sulfhydryl groups. We also include a model featuring a triply protonated carbide. The results are only mildly dependent on the QM-region size. The three most stable **E_3** isomers at the r^{2}SCAN level of theory have in common: an open belt sulfide-bridge (terminal sulfhydryl group on Fe6) and either 2 bridging hydrides (between Fe2 and Fe6), 1 bridging-1-terminal hydride (around Fe2 and Fe6) or a dihydrogen ligand bound at the Fe2 site. Analyzing the functional dependency of the results, we find that functionals previously found to predict accurate structures of spin-coupled Fe/Mo dimers and FeMoco (TPSSh, B97-D3, r^{2}SCAN, and B3LYP*) are in generally good agreement about the stability of these 3 **E_3** isomers. However, B3LYP*, similar to its parent B3LYP method, predicts a triply protonated carbide isomer as the most stable isomer, an unlikely scenario in view of the lack of experimental evidence for carbide protonation occurring in reduced FeMoco states. Distinguishing further between the 3 hydride isomers is difficult and this flexible coordination nature of hydrides suggests that multiple hydride isomers could be present during experimental conditions. N_2 binding was explored and resulted in geometries with 2 bridging hydrides and N_2 bound to either Fe_2 or Fe_6 with a local low-spin state on the Fe. N_2 binding is predicted to be mildly endothermic, similar to the **E_2** state, and it seems unlikely that the **E_3** state is capable of binding N_2.

Received 10th March 2023,
Accepted 20th July 2023

DOI: 10.1039/d3cp01106b

rsc.li/pccp

Introduction

The nitrogenase enzymes are responsible for the reduction of dinitrogen to ammonia in a complex 2-protein system that consists of the Fe protein and the MoFe protein (in the more active and better understood Mo nitrogenase).[1–6] These proteins contain multiple iron–sulfur clusters that are responsible for electron-transfer that end up in the active-site iron-molybdenum cluster, FeMoco (a [$MoFe_7S_9C$] cluster), where dinitrogen binding and reduction occurs. Despite decades of detailed kinetic and spectroscopic studies, crystallography and theoretical studies, there is no consensus on a detailed reaction mechanism. Part of the complexity comes from the nature of multi-electron reduction of N_2 substrate to the product NH_3, which the enzyme accomplishes by an 8-electron mechanism:[1–6]

$$N_2 + 8e^- + 8H^+ + 16MgATP \rightarrow 2NH_3 + H_2 + 16MgADP \quad (1)$$

where 1 molecule of H_2 is an obligatory product for every 2 NH_3 formed. The H_2 formation is nowadays known to be a critical mechanistic step, involving hydrides, as N_2 binds to a reduced state of the MoFe protein.[7–9] Electrons and protons are shuttled *via* the Fe protein to the MoFe protein (accumulating at the

[a] *College of Chemistry, Beijing Normal University, 100875, Beijing, China*
[b] *Max-Planck Institute for Chemical Energy Conversion, Stiftstrasse 34-36, 45470 Mülheim an der Ruhr, Germany*
[c] *Univ. Grenoble Alpes, CNRS, CEA, IRIG, Laboratoire de Chimie et Biologie des Métaux, 17 Rue des Martyrs, F-38054 Grenoble, Cedex, France. E-mail: ragnar.bjornsson@cea.fr*

† Electronic supplementary information (ESI) available: Additional information on QM-regions, electronic structure analysis, orbitals, geometries, broken-symmetry states, relative energies. Coordinates of QM-regions included as a ZIP-archive of XYZ-files. See DOI: https://doi.org/10.1039/d3cp01106b

FeMoco cluster), converting the resting $S = 3/2$ $\mathbf{E_0}$ form[10–13] of the cofactor to alternative redox states with integer-spin states ($\mathbf{E_1}$, $\mathbf{E_3}$) or non-integer spin-states ($\mathbf{E_2}$, $\mathbf{E_4}$). Much of our current knowledge of the cofactor comes from studies of the resting-state $\mathbf{E_0}$ form due to high-quality crystallographic studies[10–15] and EPR spectroscopic studies[10–13] and the fact that pure $\mathbf{E_0}$ samples can be prepared. Less is known about the EPR-silent $\mathbf{E_1}$ state although recent X-ray absorption and Mössbauer studies have considerably added to our knowledge.[16–18] The EPR-active $\mathbf{E_2}$ state can be studied (though low populations in samples is a problem) due to unique $S = 3/2$ signals that can be distinguished from $\mathbf{E_0}$ and it is known to relax back to $\mathbf{E_0}$ by H_2 evolution under low electron-flux conditions.[1,13,19–22] Detailed kinetic and EPR/ENDOR spectroscopic studies of the $\mathbf{E_4}$ state have revealed the occurrence of 2 hydrides.[8,9,23] N_2 binding has been shown to occur in this state, accompanied by obligatory H_2 formation which has been proposed to occur by a reductive elimination mechanism.[1,7–9]

Since the original seminal work by Thorneley and Lowe, the $\mathbf{E_3}$ state has been part of the kinetic schemes of nitrogenase such as the one shown in Fig. 1, yet very little is actually known about this state.[1,7–9,24] The original Thorneley-Lowe model suggested N_2 could bind to either $\mathbf{E_3}$ or $\mathbf{E_4}$ but that $\mathbf{E_4}$ was the state for which N_2 reduction could occur from.[1,24] Since then, regrettably, very little additional knowledge has emerged on the identity or reactivity of this state. Direct spectroscopic or kinetic determinations of $\mathbf{E_3}$ are mostly absent as mentioned in recent reviews on the spectroscopy and substrate reductions of nitrogenase.[5,6] This is due to its lack of a Kramers EPR signal from an integer-spin cluster. $\mathbf{E_3}$ was once attributed to a spectroscopic signal,[5,13] however, that is now known to be an EPR signal from $\mathbf{E_2}$. Kinetic studies on acetylene reduction in native MoFe protein and variants have suggested inhibition by N_2 at the $\mathbf{E_3}$ redox level, however, the evidence for $\mathbf{E_3}$ involvement in these reactions is indirect.[25,26]

Computational studies of FeMoco offer the opportunity to fill in these types of gaps in the experimental literature. Unfortunately, FeMoco is arguably the most challenging enzyme cofactor known in biology featuring 8 open-shell metal ions spin-coupled to an $S = 3/2$ spin state. Considerable effort has been spent on detailed electronic structure investigations into the resting $\mathbf{E_0}$ state. There is some consensus on the overall redox state as well as individual oxidation states although the electronic structure is still deeply complicated and a detailed understanding and connection to the magnetic spectroscopy literature remains elusive. The determination of the interstitial atom of FeMoco (as carbide),[15,27] the high-resolution X-ray crystal structure[15] as well as new determinations of metal oxidation states of the cofactor[27–30] have inspired multiple computational studies (or joint experimental-computational) into reduced states of FeMoco[9,18,31–37] and attempts to understand the mechanism of nitrogen binding and reduction at FeMoco.[32,34,38–50] Special efforts have been devoted to studies of the $\mathbf{E_4}$ state, known to contain 2 bridging hydrides.[9,32–35]

Considerably fewer studies have considered the structural possibilities in the $\mathbf{E_3}$ redox state, due no doubt to the lack of experimental data to compare to. In a systematic computational study by Cao and Ryde multiple structural possibilities were considered at the QM/MM level for various reduced states ($\mathbf{E_1}$–$\mathbf{E_4}$) of FeMoco, including $\mathbf{E_3}$.[31] The most favorable $\mathbf{E_3}$

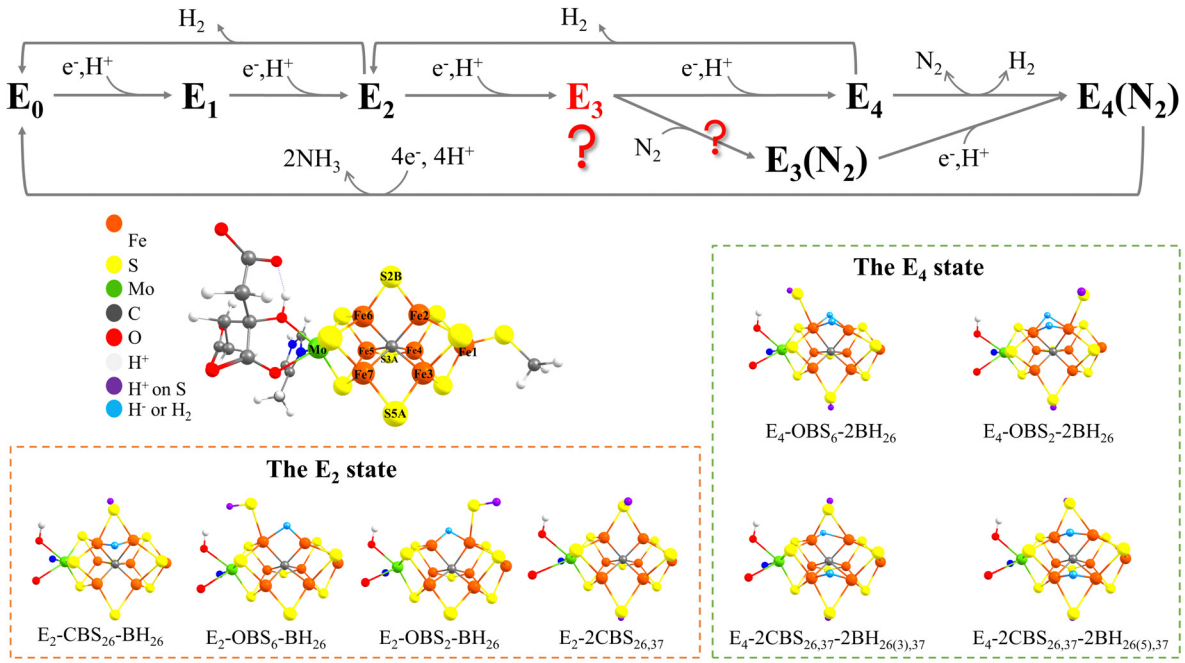

Fig. 1 The Thorneley-Lowe kinetic scheme relating $\mathbf{E_0}$, $\mathbf{E_1}$, $\mathbf{E_2}$, $\mathbf{E_3}$ and $\mathbf{E_4}$ redox states.[24] N_2 binding to $\mathbf{E_3}$ was originally suggested in the work by Thorneley and Lowe but the claim has not been substantiated. Also shown are recent suggested computational models for the $\mathbf{E_2}$ and $\mathbf{E_4}$ redox states.[9,34–37]

isomers found in that study consisted of both bridging and terminal hydrides as predicted by the TPSS functional or a triply carbide ion as predicted by B3LYP. A very recent study, also by Ryde and coworkers, suggests a model containing two bridging hydrides between Fe2 and Fe6 as the most favourable when using TPSS, r^{2}SCAN, and TPSSh functionals, while B3LYP predicts a model containing a triply protonated carbide as the lowest-energy model.[51] Additionally, Dance has studied the $\mathbf{E_3}$ redox state with large QM-cluster calculations and found the most favorable isomer to contain dihydrogen bound to the Fe6 site with a closed protonated belt sulfide-bridge and a model consisting of two terminal/bridging hydrides and an open belt sulfide-bridge.[33]

Overall, previous experimental and computational work strongly implies the existence of 1 hydride in the $\mathbf{E_2}$ state[13,19–21,31,33,36,37] and direct ENDOR-observation has convincingly demonstrated the existence of 2 hydrides (and 2 sulfur-bound protons) in the $\mathbf{E_4}$ state.[8,9,23] It seems likely to assume that the $\mathbf{E_3}$ redox state bears a structural similarity to either $\mathbf{E_2}$ or $\mathbf{E_4}$, however, it is not obvious whether the state should contain 1 or 2 hydrides. A single hydride $\mathbf{E_3}$ isomer would suggest a highly simplified electron-counting scheme of 2 electrons present in the hydride and 1 electron in the Fe part, while a 2-hydride isomer implies 4 electrons associated with the hydrides and an oxidized Fe part.

We have previously shown that the binding affinity of N_2 at an Fe site in FeMoco depends strongly on the number of hydrides bound to the Fe (which appears to be connected to the ability of the Fe site to acquire a low spin-state).[50] The question of whether the $\mathbf{E_3}$ state is capable of N_2 binding or not may be related to the number and coordination of hydrides present in the structure.

In this study we systematically study the energy landscape of the $\mathbf{E_3}$ state by a previously established computational approach that combines QM/MM methodology to reliably treat the protein environment and previously benchmarked DFT methods together with large triple-zeta basis sets and inclusion of scalar relativistic effects and dispersion corrections. We compare 3 categories of $\mathbf{E_3}$ isomers: 1-hydride isomers, 2-hydride isomers with an open belt sulfide-bridge and 2-hydride isomers with a closed belt sulfide-bridge, and a model featuring a triply protonated carbide is also included. We test 35 broken-symmetry states for 3 different spin multiplicities for each isomer with a small QM-region and the r^{2}SCAN density functional. We assess the reliability of the resulting energy ranking of isomers by comparing results using small and large QM-regions, and discuss the functional dependency of the results. Finally, we discuss the electronic structure of the most stable isomers as well as the possibility of N_2 binding to $\mathbf{E_3}$.

Computational details

Our QM/MM model is partially based on the model we previously used to study $\mathbf{E_0}$, $\mathbf{E_1}$, $\mathbf{E_2}$, and $\mathbf{E_4}$ states of FeMoco.[18,34,36,52–56] However, in this work, as in a recent study on N_2 binding to these redox states,[50] we utilize a model of the full solvated protein consisting of 320817 atoms in total. An active region of 993 atoms, centered on one of the FeMoco active sites, is used. There are 59 atoms (link-atoms included) in the small QM-A region that consists of FeMoco, sidechains of α-Cys275, α-His442, the singly protonated homocitrate ligand[52,57,58] attached to Mo, three additional hydrogens compared to the $\mathbf{E_0}$ state, and two added link-atom hydrogens. The QM-region is visualized in Fig. S1 in the ESI.† The QM-B region (145 atoms in total; link-atoms included) contains eight more residues than the QM-A region: α-Val70, α-Arg96, α-Gln191, α-His195, α-Ser278, α-Glu380, α-Phe381, and α-Arg359. In the QM-C region, there are 191 atoms (link-atoms included) and 12 more residues (10 H_2O molecules, α-Gly356, and α-Gly357) than the QM-B region (see Fig. S1 in Section 1 of the ESI†). The 10 water molecules included are present in the X-ray structure,[15] as shown in Fig. S2 of the ESI.† The α-His195 residue is described as singly protonated on N_ε (see Fig. S1 in the ESI†).

As discussed in our recent study,[50] the use of these QM-A, QM-B, and QM-C regions (same as the QM-I, QM-V, and QM-VI regions, respectively, in that article) converge quite well for reaction energies with even the small and cheap QM-A region being capable of fairly accurate results compared to the larger and more expensive QM-C region (see Table S2 of the ESI† in that article[50]).

In this work we used the QM-A region to systematically explore all considered $\mathbf{E_3}$ models (Fig. 2) in three spin states (M_S = 0, 1 and 2) and 35 BS solutions per spin state. Different orientations of protons on bridging or terminal sulfhydryl groups S2B and S5A were investigated using the lowest-energy state of each model with the QM-A region (see Section 7 in the ESI†). The QM-B region was then used to optimize the lowest-energy state for each model based on the QM-A data (the lowest-energy orientation for protons on sulfides). Finally, single-point calculations using the QM-C region were performed on top of QM-B region optimized geometries in order to evaluate the most accurate relative energies of $\mathbf{E_3}$ isomers. Broken-symmetry states of FeMoco were systematically investigated by considering all possible 35 BS solutions that can be obtained by flipping 3 of 7 open-shell Fe ions, following the original work by Noodleman and coworkers.[59,60] We note that the open-shell Mo(III) ion (present in an unusual non-Hund configuration[28]) is part of the spin-coupling problem but the configuration arises naturally during the SCF procedure. The BS states were obtained by converging first the high spin state (M_S = 34/2) of FeMoco and then flipping the spin-density of three selected Fe ions (using a procedure present in ORCA), and finally converging the SCF to the desired state. For example, BS147 (M_S = 2) is found by flipping the Fe1, Fe4, and Fe7 to be down spin and converging to M_S = 2. Additional information on BS states is included in Section 8 of the ESI.†

The QM/MM program ASH,[61] developed in our group, was used. It has a flexible interface to the OpenMM molecular mechanics library[62] and the ORCA quantum chemistry code.[63] The CHARMM36 force field[64] and standard electrostatic embedding QM/MM with link atoms as well as a charge-

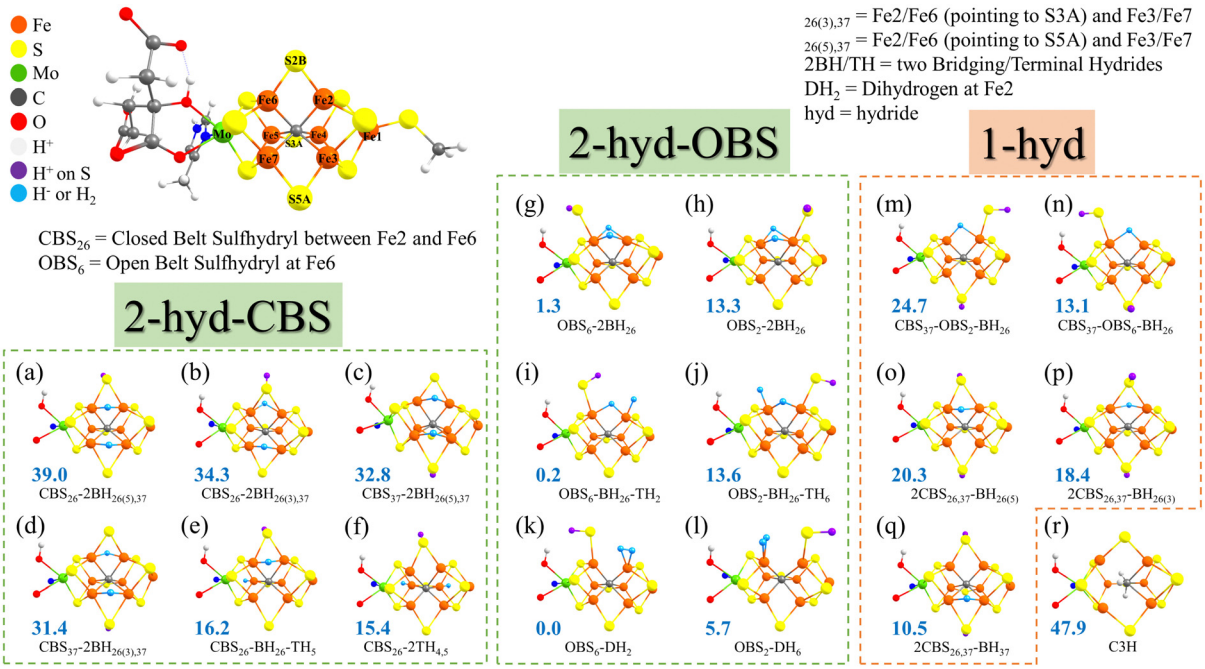

Fig. 2 The eighteen structural models for the $\mathbf{E_3}$ state that were systematically explored in this work, divided into categories of 2-hyd-CBS (2 hydrides with a closed belt sulfide bridge), 2-hyd-OBS (2 hydrides with an open belt sulfide bridge), 1-hyd (single hydride) and finally the sole protonated carbide model (r). Also shown are relative QM/MM energies (lowest-energy BS state and spin state) in blue, calculated using the r^{2}SCAN functional and the small QM-A region. All the models are isomers of the common $\mathbf{E_3}$ redox state surface. The lowest-energy spin state and BS state of **a–r** isomers are BS245 (M_S = 1), BS137 (M_S = 1), BS345 (M_S = 1), BS345 (M_S = 1), BS236 (M_S = 2), BS345 (M_S = 2), BS347 (M_S = 1), BS2356 (M_S = 0), BS235 (M_S = 2), BS147 (M_S = 1), BS147 (M_S = 1), BS346 (M_S = 2), BS147 (M_S = 1), BS247 (M_S = 2), BS14 (M_S = 2), BS14 (M_S = 2), BS346 (M_S = 2), and BS125 (M_S = 1), respectively.

shifting scheme[65] were utilized as in our previous papers.[18,34,36,52–56] Geometry optimizations were performed using an interface to the geomeTRIC optimization library[66] using HDLC internal coordinates.[67]

Four density functionals: r^{2}SCAN,[68] TPSSh,[69,70] B97-D3,[71–73] and B3LYP*[74,75] were primarily used in this work to evaluate the functional dependency of the isomer energies (Results and Discussion section C). This choice is based on a recent benchmarking study on the geometries of spin-coupled iron–sulfur dimers and FeMoco compared to high-resolution X-ray crystallographic data.[56] These 4 functionals emerged as the most reliable for Fe–Fe and Mo–Fe distances and as discussed, this was found to be primarily related to the covalency of the bridging M–S bonds between metal ions. The r^{2}SCAN functional was the most reliable functional in that study[56] (though only marginally) and it was subsequently used in our recent study on N_2 binding to multiple redox states of FeMoco.[50] In this work we used r^{2}SCAN for all QM-A region geometry optimizations when evaluating models for $\mathbf{E_3}$ in all three spin states and 35 BS solutions (Results and Discussion section B). The five lowest-energy states were then selected for each model and were QM/MM optimized using the same QM-A region with the other functionals (Results and Discussion section C). To further analyze the functional dependency we have also included results using B3LYP[76–78] and TPSS[69] and this is discussed in Section 9 of the ESI.†

An all-electron scalar relativistic treatment (ZORA[79]) with recontracted segmented triple-zeta basis sets was used in this study, which has been shown to be close to the all-electron scalar relativistic basis set limit of structures of iron–sulfur compounds.[56] The D4 dispersion correction[80,81] was used in all calculations involving r^{2}SCAN, TPSS and TPSSh while the B97-D3 and B3LYP* used the D3BJ dispersion correction (dispersion parameters for B3LYP were used). The Split-RI-J[82] approximation for Coulomb integrals was used for all functionals and additionally the semi-numerical COSX approximation for Exchange integrals (for TPSSh and B3LYP*). A decontracted auxiliary basis set by Weigend *et al.*[83,84] (named SARC/J in ORCA) was used with the RI approximation. The relativistically recontracted ZORA-def2-TZVP[83,85] basis set was used on FeMoco and additional H-atoms (compared to the $\mathbf{E_0}$ state) on FeMoco as well as the N_2 ligand in N_2-bound states while Mo used the SARC-ZORA-TZVP[86] basis set. The ZORA-def2-SVP basis set was used for other atoms in the QM region.

Relative energies were calculated from total electronic energies at 0 K. The effect of zero-point vibrational contributions on the relative energies of the lowest energy isomers was briefly investigated and the results are shown in Section 10 of the ESI;† the ZPVE effect is generally sufficiently small that it can be neglected, at least for $\mathbf{E_3}$ isomer energies. The effects of entropy were not considered in this work. For N_2 binding energies one would expect a sizeable entropy penalty associated with the free energy of binding ($\sim$10 kcal mol^{-1} based on a gas phase estimate or $\sim$ 4 kcal mol^{-1} if estimated from a diffusible position within the protein as suggested by Dance[49]) but in this work our aim is not to derive realistic estimates of the free

energy of binding. N_2 and H_2 were optimized in vacuum when calculating binding energies and dissociation energies.

Hirshfeld[87] and Mulliken[88] population analysis methods were used to derive atomic charges and spin populations. A numerical partial Hessian approach[89] was used to calculate harmonic N–N vibrational frequencies with N_2 and the binding Fe as the partial Hessian. The calculated vibrational frequencies of N_2 are shown as relative to the stretching vibration of free N_2 in the vacuum using r^{2}SCAN/ZORA-def2-TZVP (2432 cm^{-1}).

Localized orbital analysis was performed using the Pipek–Mezey method,[90] which was used to derive FeMoco electronic configurations for the lowest-energy isomers. Approximate ligand-field diagrams of Fe-bound N_2 were obtained as described in a recent study, by the combination of diamagnetic substitution, localized orbital analysis and quasi-restricted orbital (QRO) transformation.[50]

Results and discussion

We start by introducing all models considered for the $\mathbf{E_3}$ state in section A. In section B we present the results of QM/MM-calculated energies using the r^{2}SCAN density functional and a small QM-region (QM-A). In section C we explore the functional dependency of the results using 3 other density functionals (B97-D3, TPSSh and B3LYP*) while Section D compares the previous QM-A results to results calculated with the larger QM-C region. In section E we discuss the molecular and electronic structure with the help of localized orbital analysis of the 3 lowest-energy models. Finally, section F discusses N_2 binding to the $\mathbf{E_3}$ redox state and comparison is made to N_2 binding in the other $\mathbf{E_n}$ states.

A. The E_3 models investigated

The models for $\mathbf{E_3}$ discussed primarily in this work can be grouped into 3 categories as shown in Fig. 2: models with 2 hydrides with a closed belt sulfide-bridge (**2-hyd-CBS**, Fig. 2a–f), 2-hydride/H_2 models with an open belt sulfide-bridge (**2-hyd-OBS**, Fig. 2g–l) and single-hydride models (**1-hyd**, Fig. 2m–q). We also discuss a model containing a triple protonated carbide (**C3H**, Fig. 2r) for comparison as previous studies have indicated some QM protocols favouring carbide protonation in reduced FeMoco states. All 18 models contain the same number of electrons and are on the same energy surface.

Some of the 2-hydride models can be thought of as derived from $\mathbf{E_4}$ models discussed in the literature (shown in Fig. 1) but lacking an S-bound H-atom. For example, models shown in Fig. 2a–d in the **2-hyd-CBS** category are derived from $\mathbf{E_4}$ models discussed by *e.g.* Ryde, Raugei and Hoffman;[9,32,35] while models in Fig. 2g and h in the **2-hyd-OBS** category are more related to $\mathbf{E_4}$ models from our own work.[34] Ryde and coworkers also calculated models $\mathbf{CBS_{26}\text{-}2BH_{26(5),37}}$ **(a)**, $\mathbf{OBS_6\text{-}2BH_{26}}$ **(g)** and $\mathbf{OBS_2\text{-}2BH_{26}}$ **(h)** in a recent study.[51] The **1-hyd** models (**m–q**) are more similar to $\mathbf{E_2}$ models discussed in the literature[36,37] but feature an extra S-bound proton (and electron). We note that models $\mathbf{CBS_{37}\text{-}OBS_2\text{-}BH_{26}}$ **(m)**, $\mathbf{2CBS_{26,37}\text{-}BH_{26(5)}}$ **(o)**, and $\mathbf{2CBS_{26,37}\text{-}BH_{26(3)}}$ **(p)** were included in a recent study.[51]

Additionally, we include models for $\mathbf{E_3}$ suggested in the QM/MM investigations by Ryde and coworkers:[31,51] $\mathbf{CBS_{26}\text{-}BH_{26}\text{-}TH_5}$ **(e)**, $\mathbf{CBS_{26}\text{-}2TH_{4,5}}$ **(f)**, and **C3H (r)**, shown in Fig. 2e, f and r. The $\mathbf{CBS_{26}\text{-}BH_{26}\text{-}TH_5}$ model contains a protonated closed belt sulfide-bridge between Fe2 and Fe6, a bridging hydride between Fe2 and Fe6, and a terminal hydride at Fe5. The $\mathbf{CBS_{26}\text{-}2TH_{4,5}}$ also has a protonated closed sulfide-bridge but two terminal hydrides on both Fe4 and Fe5. Three hydrogens were added directly to the carbide in the **C3H** model (Fig. 2r).

We note that Dance has previously suggested $\mathbf{OBS_6\text{-}BH_{26}\text{-}TH_2}$ as a model for the $\mathbf{E_3}$ state (named **3H.2x.26.2b** in the original work).[33] For comparison we also include $\mathbf{OBS_2\text{-}BH_{26}\text{-}TH_6}$ by exchanging the sulfhydryl and hydrides positions (compare Fig. 2i and j). Dance also reported on a model with a similar hydride geometry as $\mathbf{OBS_2\text{-}BH_{26}\text{-}TH_6}$ but with a CBS configuration.[33] Such a geometry could not be stabilized by us but is discussed in the ESI† (see Fig. S4).

Models featuring a dihydrogen group in the $\mathbf{E_3}$ state have previously been speculated on[91,92] and suggested by calculations.[33,91] Inspired by $\mathbf{OBS_6\text{-}BH_{26}\text{-}TH_2}$ and $\mathbf{OBS_2\text{-}BH_{26}\text{-}TH_6}$ (Fig. 2i and j) we constructed the $\mathbf{OBS_6\text{-}DH_2}$ and $\mathbf{OBS_2\text{-}DH_6}$ models (shown in Fig. 2k and l). Dance previously suggested a model with a protonated closed sulfide-bridge (S2B) and H_2 at Fe6 as a candidate for $\mathbf{E_3}$,[33] discussed in the ESI† and shown in Fig. S5, but such a model could either not be stabilized or found to be very high in energy.

B. Energy ranking of E_3 isomers using r^{2}SCAN and the 59-atom QM-A region

The 18 $\mathbf{E_3}$ models (**a–r** in Fig. 2) were optimized by QM/MM calculations using the small QM-A region, and the r^{2}SCAN functional. For each structural isomer we explored three spin states (M_S = 0, 1, 2) and 35 possible broken-symmetry state alignments for each spin state, giving a total of 105 electronic states calculated for each structural isomer. A comparison of spin-state energies can be found in Fig. S18 for each isomer in section 8 of the ESI† and we additionally show the type of BS class that tends to be the most favorable in Table S10 (ESI†). While here we opted to systematically study the BS-state problem rigorously, it appears that for the hydride-based isomers in this work it may be sufficient for future studies to primarily focus on the BS7, BS8 and BS10 classes of broken-symmetry solutions (and to a lesser extent BS6 and BS9). Furthermore Section 12 of the ESI† shows the energies and spin populations of every BS-state calculated for each isomer.

Fig. 2 shows the relative QM/MM energy of the lowest state calculated for each isomer. The **C3H** model (Fig. 2r) containing a triply protonated carbide, previously discussed by Ryde and coworkers,[31] is predicted to be much higher than other isomers and would seemingly be ruled out at the r^{2}SCAN level of theory (note that Section C discusses the functional sensitivity of this model). Comparing the 3 different categories of hydride-based $\mathbf{E_3}$ models, it is clear that **2-hyd-CBS** models are predicted to be in general higher in energy than models from the other

categories, featuring both the highest-energy structural isomers in the comparison (*e.g.* structures in Fig. 2a–d, >30 kcal mol^{-1}) and the lowest-energy structures (shown in Fig. 2e and f) are 15–16 kcal mol^{-1} higher in energy than the lowest-energy isomer (Fig. 2k). The lowest-energy isomers in the **2-hyd-CBS** category, featuring either terminal or bridging hydrides: **CBS$_{26}$-BH$_{26}$-TH$_5$** and **CBS$_{26}$-2TH$_{4,5}$** were previously suggested by Ryde and coworkers.[31] Interestingly, the **E$_3$** models (**a**–**d**) inspired by some previous **E$_4$** models[9,32,35] are here predicted to be very high in energy (31–39 kcal mol^{-1}).

The single-hydride **1-hyd** isomers are on average lower in energy than the **2-hyd-CBS** isomers but are still at least 10 kcal mol^{-1} above the lowest energy isomer (Fig. 2k) in the **2-hyd-OBS** category. The most favorable **1-hyd** isomer features a bridging hydride between Fe3 and Fe7 and with 2 protons on S2B and S5A.

The overall stability of the isomers in the **2-hyd-OBS** category suggests an overall improved thermodynamic preference associated with an isomer having 2 hydrides instead of just 1, but only if those hydrides are allowed more flexible coordination, here by having an open belt sulfide-bridge (*i.e.* protonated S2B converting to a terminal sulfhydryl group on Fe2 or Fe6). This improved stability of hydride-based isomers upon allowing a protonated belt sulfide to become a terminal sulfhydryl group, is consistent with our previous work on the **E$_2$** and **E$_4$** states.[34,36]

Three **2-hyd-OBS** models emerge overall as the lowest in energy: **OBS$_6$-DH$_2$** (lowest), **OBS$_6$-BH$_{26}$-TH$_2$** (+0.2 kcal mol^{-1}) and **OBS$_6$-2BH$_{26}$** (+1.3 kcal mol^{-1}). These 3 models have a terminal sulfhydryl group on Fe6 in common but differ in terms of the precise H-atom coordination. **OBS$_6$-DH$_2$** furthermore differs where the H-atoms have merged to form an H$_2$ ligand bound side-on to Fe2.

Symmetrically related versions of these 3 models are: **OBS$_2$-DH$_6$**, **OBS$_2$-BH$_{26}$-TH$_6$** and **OBS$_2$-2BH$_{26}$**; they are, however, not as stable, due to the position of the sulfhydryl group on Fe2 instead of Fe6. This causes a steric clash with the His195 residue as confirmed by comparison with simple cluster-continuum calculations (Fig. S3 in the ESI†). We note that this preference may also be affected by the protonation state of His195 as *e.g.* discussed in recent work[50] but here we chose to model His195 as singly protonated on the N$_\varepsilon$ atom (as in the **E$_0$** state).

The results in this section differs from previous computational work on the **E$_3$** state by including more diverse isomers than were previously studied or by employing considerably different computational protocols. In previous QM/MM work by Ryde and coworkers,[31] **2-hyd-OBS** type models for **E$_3$** were simply not included (as the hemilability of protonated sulfide bridges was not known at the time). In very recent work by Jiang and Ryde,[51] the **OBS$_6$-2BH$_{26}$** model was found to be the lowest-energy model (using TPSSh, r^{2}SCAN, and TPSS) which is consistent with our results. Dance has also previously studied various **E$_3$** isomers,[33] and an **OBS$_6$-BH$_{26}$-TH$_2$** model was found by him to be the most stable, which is also consistent with our results. The **OBS$_6$-2BH$_{26}$** and **OBS$_2$-DH$_2$** isomers were not explored in Dance's work; he did, however, find a **CBS$_{26}$-DH$_6$** model to be very stable. Dance also reported that **CBS$_{26}$-BH$_{26}$-TH$_6$** is about 5 kcal mol^{-1} higher than **OBS$_6$-BH$_{26}$-TH$_2$**. Attempts at reproducing calculations on **CBS$_{26}$-DH$_6$** and **CBS$_{26}$-BH$_{26}$-TH$_6$** models (see Fig. S4 and S5 in the ESI†), however, were unsuccessful and we attribute these differences to the different computational protocols employed (QM-cluster *vs.* QM/MM and BLYP *vs.* r^{2}SCAN).

The energy of evolving H$_2$ from the **E$_3$-OBS$_6$-DH$_2$** model, *i.e.* the reaction **E$_3$-OBS$_6$-DH$_2$** $\rightarrow$ **E$_1$-S2B** + H$_2$ has an energy of -15.2 kcal mol^{-1} using the QM-A region (-9.9 kcal mol^{-1} using the QM-C region), meaning there is a reasonable driving force for **E$_3$** $\rightarrow$ **E$_1$** relaxation (this can be compared to a calculated **E$_2$** $\rightarrow$ **E$_0$** relaxation energy of -19.4 kcal mol^{-1} using a QM-C region reported in ref. 36). The enzyme would have to prevent this favorable H$_2$ relaxation process by utilizing a high electron flux rate in order to reach the **E$_4$** state (or alternatively N$_2$ binding) faster than the rate for H$_2$ evolution. Barriers for H$_2$ evolution were not calculated in this work but may be lower than that previously calculated for **E$_2$** $\rightarrow$ **E$_0$** ($\sim$21 kcal mol^{-1}[36]). It is also possible that the initial **E$_3$** state formed, right after e$^-$/H$^+$ transfer (the details of which are unknown), is not one of the favorable **2-hyd-OBS** isomers but perhaps a state closer in nature to an **E$_2$**-like isomer, perhaps one of the **1-hyd** isomers shown *e.g.* in Fig. 2n or q. The relevant rate for H$_2$ evolution may then involve complex proton and/or hydride reorganization (with unknown barriers), perhaps going from **1-hyd** $\rightarrow$ **2-hyd-OBS** or some other pathway that leads to H$_2$ evolution.

C. The functional dependency of the energy ranking

A critical part of an electronic structure study of FeMoco is the choice of methodology to describe the electronic structure. In this work we utilize a scalar relativistic (using the ZORA Hamiltonian) all-electron approach with polarized triple-zeta basis sets on all FeMoco atoms, that should result in very small basis-set incompleteness errors and no errors due to effective core potential approximations (that can be large for FeS systems as discussed in our previous benchmarking study[56]). This means that the primary error in the electronic structure comes from the use of broken-symmetry density functional theory and in particular the choice of functional. The choice of functional is critical for FeMoco chemistry as is well demonstrated for FeMoco **E$_4$** isomer energies in the work by Ryde and coworkers[35] where different non-hybrid and hybrid functionals gave completely different results for **E$_4$** isomer energies, in particular regarding the stability of hydride *vs.* protonated carbide formation.

In recent work from our group[56] we benchmarked different functionals on their ability to describe the geometries of spin-coupled Fe–Fe and Mo–Fe dimers (mostly with bridging sulfides) as well as FeMoco itself. Four functionals emerged as the most accurate: r^{2}SCAN, B97-D3, TPSSh, B3LYP*, having considerably lower errors than other non-hybrid functionals (that have a tendency to underestimate metal–metal distances) and other hybrid functionals (that have a tendency to overestimate metal–metal distances).[56] The trends in metal–metal distances were found to correlate with covalency parameters of the Fe–S bridging bonds, suggesting that the geometric errors are

reflecting directly errors made in the covalency of the metal–ligand bonds that are responsible for spin-coupling interactions in this complex spin-coupled cofactor. r^{2}SCAN was found to have a slight edge in the study and being a non-hybrid functional (lower computational cost) we used it to generate the results in section B. We note that other FeMoco studies from our group previously used TPSSh[18,28,30,34,36,52,55] while other researchers have utilized functionals such as TPSS, BP86, BLYP, PBE, B3LYP, B3LYP* and M06-2X.[9,31–33,35,37–49,58,93–99]

Here, we test whether density functionals that predict similar geometric structures of spin-coupled FeS systems (including $\mathbf{E_0}$ FeMoco), predict similar energies of FeMoco $\mathbf{E_3}$ isomers or not. We use the same QM/MM setup and same QM-region as in section B and every isomer was optimized with each functional to allow a fair comparison and to prevent bias. The five lowest-energy BS-states for each structural isomer (from the r^{2}SCAN comparison in Section B) were used in this comparison (see Section 9 in the ESI† for more information).

The results in Fig. 3 reveal overall a highly similar trend for 3 of the functionals: r^{2}SCAN, B97-D3 and TPSSh. The 3 functionals are in good agreement about the **2-hyd-OBS** isomers being more favorable than **2-hyd-CBS** as well as **1-hyd** isomers. Furthermore, these 3 functionals agree on the 3 most stable isomers: $\mathbf{OBS_6\text{-}DH_2}$, $\mathbf{OBS_6\text{-}BH_{26}\text{-}TH_2}$ and $\mathbf{OBS_6\text{-}2BH_{26}}$.

While the results for B3LYP* are somewhat similar, they differ in an important way: the carbide-protonated model **C3H** is found to be the lowest energy isomer (4.5 kcal mol^{-1} lower than $\mathbf{OBS_6\text{-}DH_2}$), in sharp contrast to r^{2}SCAN (where **C3H** is the least favorable model) and TPSSh and B97-D3 (unfavorable by 25.1 and 29.8 kcal mol^{-1}). This mild preference for carbide-protonation with B3LYP* follows the well-established preference of carbide-protonation in the $\mathbf{E_4}$ state by the regular 20% B3LYP hybrid. As shown in the ESI,† B3LYP favors the carbide-protonation in $\mathbf{E_3}$ by $\sim$20 kcal mol^{-1}. The B3LYP* result is hence not entirely unexpected (differing by 15% instead of 20% HF exchange). The B3LYP*/B3LYP results are also consistent with the recent study by Jiang and Ryde[51] where B3LYP predicts **C3H** to be the lowest energy model. Their work, however, also show TPSSh predicting the **C3H** model to be almost isoenergetic with $\mathbf{OBS_6\text{-}2BH_{26}}$ (0.9 kcal mol^{-1}). Our TPSSh results in contrast show **C3H** to be unfavorable by 25.1 kcal mol^{-1}. The reason for the difference is likely rooted in the larger basis sets (ZORA-def2-TZVP) together with a ZORA relativistic treatment used in our work, while a small def2-SV(P) basis set was used by Ryde and coworkers.[51]

In the ESI† we have included data with the non-hybrid functional TPSS for comparison (see Fig. S19 in section 9 of the ESI†). TPSS gives a slightly different picture from r^{2}SCAN,

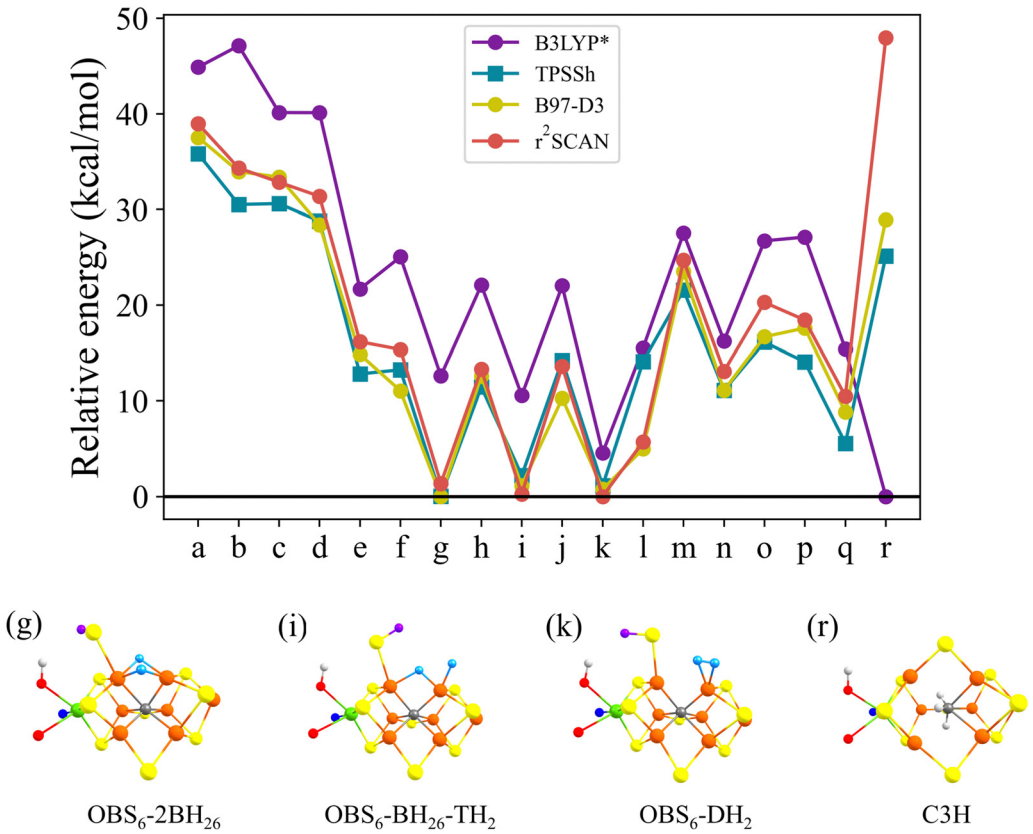

Fig. 3 A comparison of the relative energies of $\mathbf{E_3}$ isomers with different density functionals using QM-A region. The *x*-axis indicates the structural isomer from Fig. 2. r^{2}SCAN, B97-D3, TPSSh consistently predict that the 3 most stable isomers are $\mathbf{OBS_6\text{-}2BH_{26}}$,$\mathbf{OBS_6\text{-}BH_{26}\text{-}TH_2}$ and $\mathbf{OBS_6\text{-}DH_2}$ while B3LYP* favours the **r** isomer. Note that all functionals include either D3 or D4 dispersion correction (see Computational details). Information about spin states and BS solutions of each model are available in Tables S12–S29 of the ESI.†

B97-D3, and TPSSh. The functional is overall in agreement about isomers **OBS_6-$2BH_{26}$** and **OBS_6-BH_{26}-TH_2** being low-energy but predicts isomer **OBS_6-DH_2** as being considerably less stable. TPSS (like most other non-hybrid functionals) has a tendency to systematically underestimate Fe–Fe distances in spin-coupled Fe–S dimers and to give worse structures for FeMoco overall, apparently due to overestimating Fe–S bond covalency.

Overall, the results of this functional comparison show that r^{2}SCAN, B97-D3 and TPSSh functionals predict very similar energetics for $\mathbf{E_3}$ isomers. These 3 functionals have previously been found to describe well the metal–metal distances of spin-coupled iron–sulfur dimers as well as $\mathbf{E_0}$ FeMoco itself. This is despite the fairly large variability in hydride isomers (1 *vs.* 2 hydrides or Fe-bound H_2), terminal *vs.* bridging hydrides and open *vs.* closed terminal sulfide bridges. In contrast, the B3LYP* functional, which was previously[56] found to behave similarly to r^{2}SCAN, B97-D3 and TPSSh, favours the triply protonated carbide model (similar to its parent B3LYP functional).

There is no experimental evidence to suggest that the interstitial carbide ion of FeMoco can be protonated. In fact, a recent ^{13}C ENDOR study on several reduced $\mathbf{E_n}$ and ligand-bound FeMoco states shows that the carbide hyperfine coupling remains unchanged, suggesting that the carbide coordination environment remains intact, consistent with a stabilizing role of the carbide. In view of this, the prediction of protonated carbide isomers by B3LYP* (and B3LYP) likely represent artifacts from these functionals. We suggest **OBS_6-$2BH_{26}$** and **OBS_6-BH_{26}-TH_2** and **OBS_6-DH_2** models as the most likely models for the $\mathbf{E_3}$ state.

D. The QM-region size dependency of the energy ranking

Another critical aspect of modelling metalloenzymes is the treatment of the protein environment. In the QM/MM model used, the whole solvated protein is included in the calculation, however, only a small part is described by quantum mechanics (DFT) and the rest of the system is described by an MM forcefield (CHARMM36). The QM and MM subsystems interact *via* electrostatic embedding and Lennard-Jones potentials (and bonded interactions at the interface). There are always potential errors made by the definition of the QM-region, in particular residues strongly interacting with the cofactor should ideally be present in the QM-region (to avoid imperfect quantum-classical interactions). By increasing the size of the QM-region one can reduce the magnitude of such effects.

In Fig. 4 we compare the effect of using a small 59-atom QM-A region (used in Sections B and C) and using the larger 191-atom QM-C region (single-point calculations performed on the 145-atom QM-B optimized geometries). This comparison was only performed using the r^{2}SCAN functional and only for isomers **e** to **q** (see Fig. 2) as multiple functionals consistently found isomers **a–d** and **r** to be much higher in energy than other isomers in energy. The results in Fig. 4 reassuringly reveal that the energy landscape does not change very much overall and the stability of **2-hyd-OBS** isomers holds and both QM-regions predict the same 3 isomers (models **OBS_6-$2BH_{26}$ (g)**, **OBS_6-BH_{26}-TH_2 (i)** and **OBS_6-DH_2 (k)**) as the most favourable. However, the larger QM-C region slightly increases the energy gap between these 3 isomers, further stabilizing **OBS_6-DH_2** (3.1 and 3.3 kcal mol^{-1} more stable than **OBS_6-$2BH_{26}$** and **OBS_6-BH_{26}-TH_2** at the r^{2}SCAN level).

Considering both the functional and the QM-region dependency we conclude that the **OBS_6-DH_2**, **OBS_6-BH_{26}-TH_2** and **OBS_6-$2BH_{26}$** are consistently predicted to be the most stable $\mathbf{E_3}$ isomers. The dihydrogen isomer (**OBS_6-DH_2**) is predicted to be the most stable, with the energy gap differing depending on precisely which functional and QM-region are used. However, there is certainly uncertainty associated with these energies and we suggest any of these 3 isomers is likely to be encountered

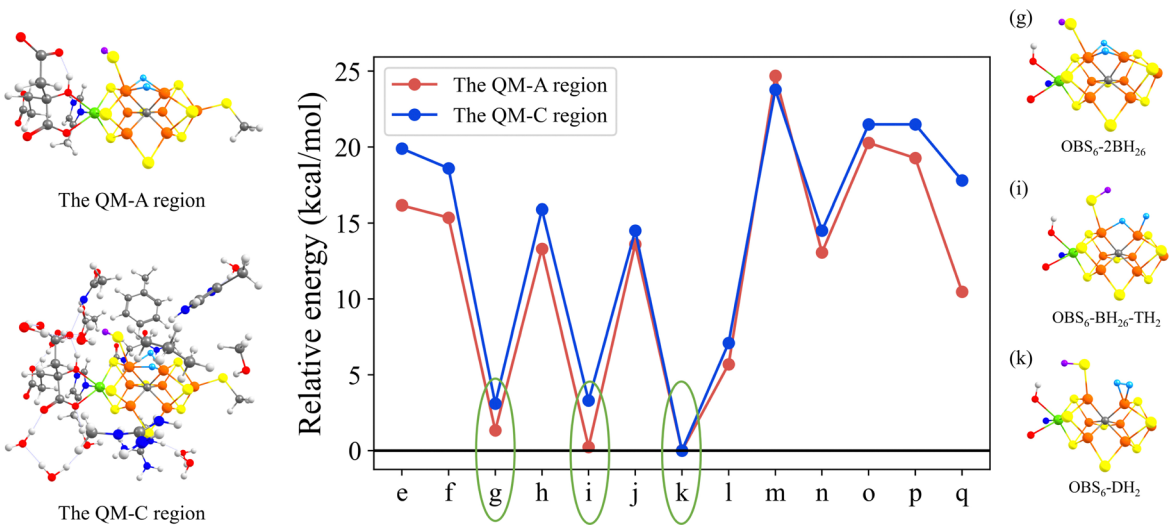

Fig. 4 The comparison of relative QM/MM energies using r^{2}SCAN for models (**e**–**q**) between using the QM-A and QM-C regions. The labels of the *x*-axis indicate the models defined in Fig. 2. QM-A region contains 59 atoms while QM-C contains 191 atoms. The spin states and BS solutions are the same as Fig. 2.

experimentally. In order to check whether these 3 isomers might be distinguished by other factors we performed additional calculations for these 3 isomers (see Section 10 in the ESI†) where we checked how much the D4 dispersion correction plays a role (a very small effect of 0.1–0.3 kcal mol^{-1}) and whether inclusion of a zero-point vibrational energy (ZPVE) correction would affect the energy ordering. The ZPVE correction was also found to be relatively small in magnitude, ~0.7 kcal mol^{-1} (see Section 10 in the ESI†).

E. The electronic structure of the 3 lowest energy isomers

Comparing the geometric features of the common [Fe_2H_2C] core of these isomers reveals interesting differences (see Fig. 5) when evaluated using the r^{2}SCAN functional and QM-region C. The Fe2–Fe6 distance is considerably shorter in the **OBS$_6$-2BH$_{26}$** isomers (2.41 Å) than in the **OBS$_6$-BH$_{26}$-TH$_2$** (2.68 Å) and **OBS$_6$-DH$_2$** (2.63 Å), a geometric feature likely a result of the 2 bridging hydrides. There are also considerable changes in Fe–C bond lengths in these 3 isomers, suggesting that the carbide might be pushing electron density to different degrees depending on the hydride/H_2 coordination. The Fe–H distances of the bridging hydrides are generally shorter for Fe2 than for Fe6 in **OBS$_6$-BH$_{26}$-TH$_2$** and **OBS$_6$-2BH$_{26}$**, that suggest that these hydrides are not equally shared between Fe ions. The Fe2–H distances in **OBS$_6$-DH$_2$** are considerably longer (1.71 Å) than the Fe–hydride distances, and with a relatively short H–H distance of 0.84 Å, a dihydrogen ligand description seems appropriate.

The electronic structure of these 3 isomers is also compared in Fig. 5 by electronic configuration diagrams derived from localized orbital analysis of the broken-symmetry determinants. The **E$_3$** state has three more e^-/H^+ pairs than the **E$_0$** state, having 22 d-electrons and 19 d-electrons in the Fe_4 sub-cubane and $MoFe_3$ sub-cubane, respectively. Analogous electron configuration diagrams for **E$_0$** are found in Fig. S11 in the ESI† for comparison. In **OBS$_6$-DH$_2$**, we find that two additional electrons are present in the form of the H_2 ligand while an additional localized electron is present on Fe2 (suggesting a high-spin ferrous ion). **OBS$_6$-BH$_{26}$-TH$_2$** and **OBS$_6$-2BH$_{26}$** models have interestingly very similar electronic structures which offers a possible explanation for the very similar energies for these isomers. This is despite the different hydride coordination and the different Fe2–Fe6 distance. Unlike the dihydrogen isomer, 4 electrons are associated with the H-atoms, with localized orbitals indicating considerable Fe-character. Interestingly, there is an unusual electronic configuration for Fe2: most of the Fe-character in the hydride orbitals is associated with Fe2 rather than Fe6, which together with the asymmetric Fe–H distances previously discussed, suggests that these hydrides are not completely bridging (see localized orbital visualizations in Fig. S14 of the ESI†). The use of 4 electrons to stabilize the Fe–H bonds at first glance suggests that the cofactor has been effectively oxidized but the strong covalency of the Fe–H bonds in these states makes it difficult to make a clear assignment of oxidation states.

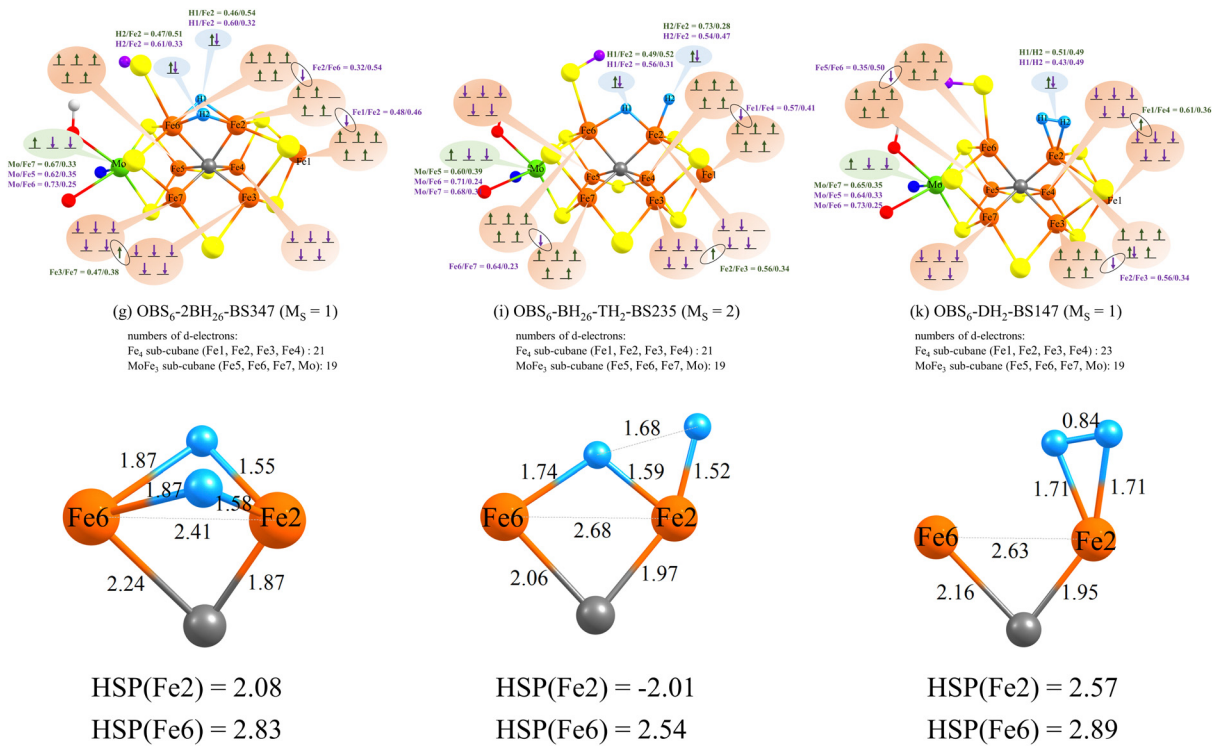

Fig. 5 Top: Electronic configurations of **OBS$_6$-2BH$_{26}$**, **OBS$_6$-BH$_{26}$-TH$_2$** and **OBS$_6$-DH$_2$** derived from localized orbital analysis of the QM/MM calculation using r^{2}SCAN and the QM-C region. The spin states and BS solutions of these three isomers are the same as Fig. 4. The localized orbitals of these three models are shown in Fig. S12–S14 in the ESI.† The green and purple numbers indicate localized orbital populations of Mo, Fe and H-atoms. Bottom: Close-up of the geometries associated with the Fe–H interactions at Fe2 and Fe6. HSP(atom) indicates the Hirshfeld spin populations of Fe2 and Fe6.

The comparison of electronic configurations and geometries for different functionals (B3LYP*, TPSSh, B97-D3, r^{2}SCAN, and TPSS) is shown in Fig. S20 to S25 in the ESI.† The five functionals give similar electronic configurations and geometries for **OBS$_6$-DH$_2$**. For **OBS$_6$-BH$_{26}$-TH$_2$**, B3LYP*, TPSSh, B97-D3 give a similar description as r^{2}SCAN, with an electron-deficient Fe_4 subcubane, but TPSS in contrast predicts an electron-deficient $MoFe_3$ sub-cubane. The electronic structure of the **OBS$_6$-2BH$_{26}$** isomer is more complex; B3LYP* predicts similar electronic and geometric structures to r^{2}SCAN, and two bridging hydrides share four electrons with Fe2, correlating with shorter Fe2-hydride distances than Fe6-hydride (see Fig. S21, ESI†), and one electron has moved from the Fe_4 sub-cubane to the hydrides (compared to the **E$_0$** state, see Fig. S11, ESI†). In contrast, TPSSh predicts four electrons associated with Fe6–H bonds which correlates with shorter Fe6–H distances than Fe2–H distances, and an electron-deficient $MoFe_3$-cubane. TPSS and B97-D3 behave intermediate to the other functionals, predicting four almost equally shared electrons between Fe2 and Fe6, resulting in similar Fe2–H and Fe6–H distances and unusually Fe2 and Fe6 share an electron.

These geometric differences and electronic structure analysis clearly reveal a complex electronic structure which is not easily understood at present, requiring further studies. Also, despite similar energetics predicted by the different functionals (see Fig. 3), the electronic structure from different functionals is not always similar.

F. N_2 binding to the E_3 state

The original kinetic model by Thorneley and Lowe[1,24] suggested N_2 binding to the **E$_3$** state, although little additional data has since appeared to support or refute that hypothesis. The Fe2–Fe3–Fe6–Fe7 face has long been suggested as a site for N_2 binding, primarily based on mutation studies.[100,101] Additionally, crystallographic studies[102–104] have shown displacement of the bridging sulfide (S2B) between Fe2 and Fe6 under certain conditions, which further implicates Fe2 or Fe6 as a likely site of ligand binding.[105,106] A recent X-ray structure study[104] appeared to show N_2 replacing three possible sulfur sites (S2B, S3A and S5A) but this claim is controversial.[107–109] Regardless of the precise interpretations of recent crystal structures, Fe2 and Fe6 are likely binding sites for N_2.

In previous work from our group[34,50] we showed how calculations of N_2 binding to Fe sites (specifically Fe2 and Fe6) at FeMoco is almost always connected with the formation of local low-spin states of Fe and furthermore hydrides appear to aid in the formation of such states, offering a possible explanation for why the **E$_4$** state has an improved affinity for N_2.

As the results in this work suggest **OBS$_6$-DH$_2$**, **OBS$_6$-BH$_{26}$-TH$_2$** and **OBS$_6$-2BH$_{26}$** as plausible models for the **E$_3$** state, and with all 3 models featuring either 2 hydrides or an Fe-bound H_2 it is interesting to consider whether N_2 binding might be favored to these **E$_3$** isomers or not. As **OBS$_6$-2BH$_{26}$** has a more obvious accessible binding site, we focused primarily on this isomer.

We systematically investigated N_2 binding to Fe2 of **OBS$_6$-2BH$_{26}$** or Fe6 of **OBS$_2$-2BH$_{26}$** in three spin states (M_S = 0, 1, 2) and 35 BS solutions using the QM-A region, and the binding energies are shown in Fig. S15 in the ESI.† The QM-A region was then expanded to the QM-C region, and the binding energies of N_2 to Fe2 or Fe6 were found to be +1.5 and +1.9 kcal mol^{-1} (relative to **OBS$_6$-DH$_2$**), respectively, shown in Fig. 6, which is

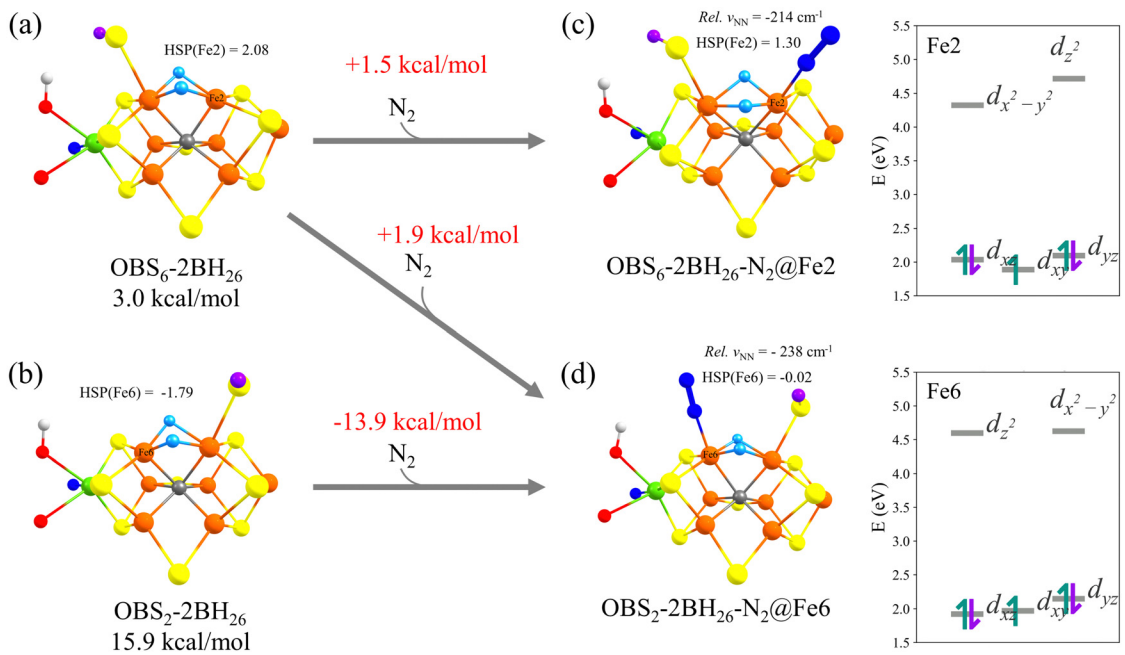

Fig. 6 N_2 binding energies using the QM-C region and r^{2}SCAN. Also shown are relative N–N frequencies for N_2 (relative to free N_2: 2432 cm^{-1}), Hirshfeld spin populations and quasi-restricted orbital (QRO)-based ligand field diagrams of binding site Fe. The N_2@Fe2 and N_2@Fe6 have a spin state of M_S = 0 and BS states of BS147 and BS234, respectively. The spin states and BS solutions of (a) and (b) are BS347 (M_S = 1) and BS2356 (M_S = 0), respectively.

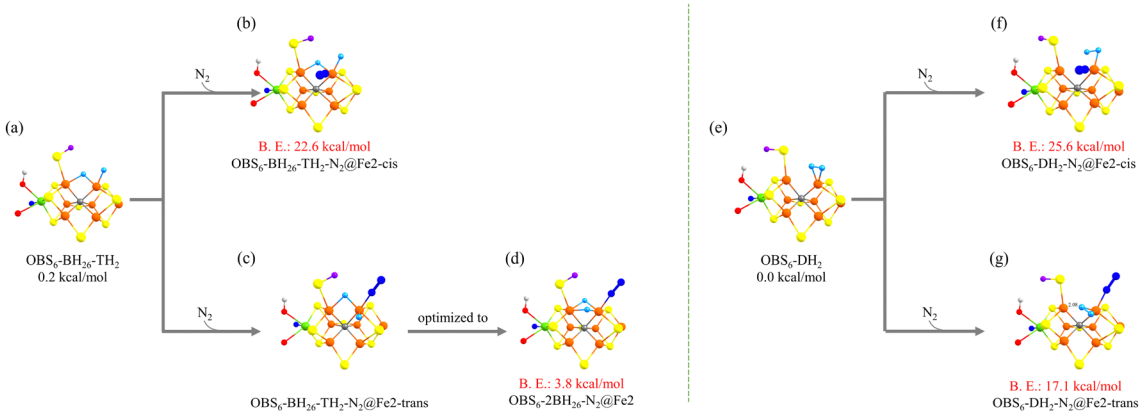

Fig. 7 The binding energies (B. E.) of N_2 binding to **OBS_6-BH_{26}-TH_2** and **OBS_6-DH_2** (using the QM-A region and r^{2}SCAN), which are relative to the lowest-energy isomer **OBS_6-DH_2** (Fig. 2k). The BS states of (b), (d), (f), and (g) are BS156, BS147, BS156, and BS157, respectively, and all these states are in low spin (M_S = 0). Note the energy shown in (d) differs from Fig. 6, due to different QM regions.

similar to the r^{2}SCAN results reported by Ryde and coworkers.[51]

We note that Dance previously found the **OBS_6-$2BH_{26}$-N_2@Fe2** isomer by binding N_2 to **CBS_{26}-BH_{26}-TH_6** (unstable in the present study; see Fig. S4 in the ESI†), and reported that there is a barrier of 9 kcal mol^{-1} to making the terminal hydride become bridging.[38,42]

The direct binding of N_2 *via* **OBS_2-$2BH_{26}$ → OBS_2-$2BH_{26}$-N_2@Fe6** is much stronger (−13.9 kcal mol^{-1}) but the **OBS_2-$2BH_{26}$** isomer is higher in energy due to clashes of the terminal sulfhydryl group with the His195 residue. The addition of a translational entropy penalty would make this binding even more unfavourable and hence unlikely to occur.

Dance suggested that an H_2 ligand can enhance N_2 binding to Fe.[43,44] Therefore, we additionally explored N_2 binding to **OBS_6-DH_2**, and N_2 binding to **OBS_6-BH_{26}-TH_2** was also attempted for completeness. N_2 binding scenarios where N_2 binds directly to Fe2 in the **OBS_6-BH_{26}-TH_2** and **OBS_6-DH_2** isomers were studied in either a *cis* or *trans* orientation relative to the Fe2–carbide bond. These calculations were performed using the QM-A region and we investigated only the low spin state (M_S = 0) and we restricted the broken-symmetry state comparison to the BS6 class of solutions (BS156, BS157 and BS167) and the BS10 class of solutions (BS125, BS127, BS135, BS136, BS146 and BS147) as these were the lowest-energy BS states for the N_2-bound isomers of **OBS_6-$2BH_{26}$-N_2@Fe2** and **OBS_2-$2BH_{26}$-N_2@Fe6** (see Fig. S15 and Table S10, ESI†). The results in Fig. 7b reveal that N_2 binding to Fe2 in **OBS_6-BH_{26}-TH_2** in a *cis* orientation relative to the Fe2–C bond results in a stable N_2-bound minimum but with an unfavourable binding

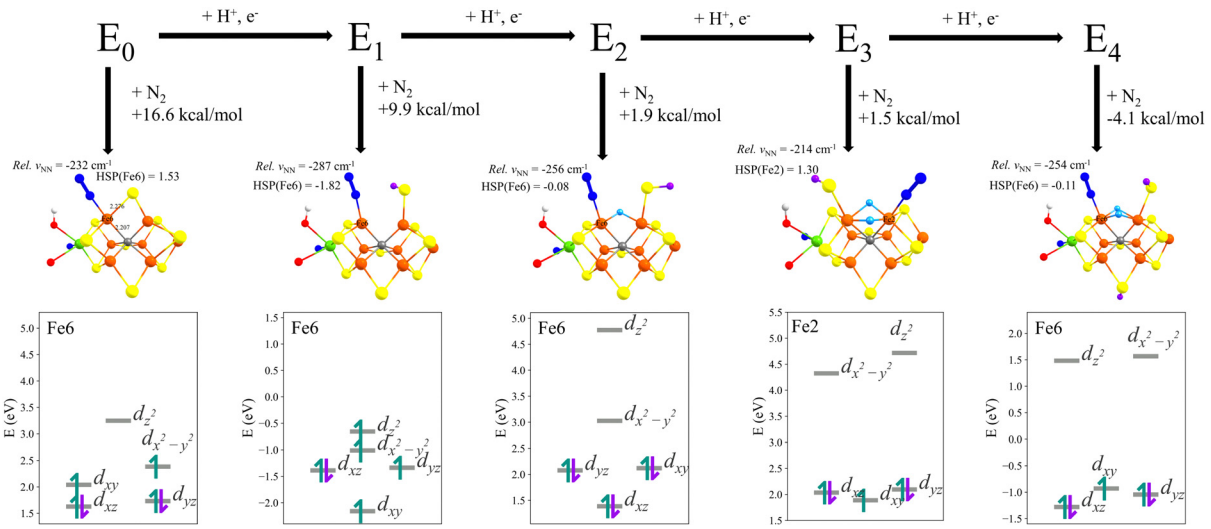

Fig. 8 The trend of N_2 binding energies in going from models of **E_0** to **E_4** states according to calculations from previous work[50] and this work (using r^{2}SCAN). Also shown are approximate ligand-field diagrams, derived from a combination of localized-orbital analysis and QRO MO energies from a diamagnetically substituted model (see ref. 50). The results for the **E_3** state were calculated using the QM-C region that is the same as the QM-VI region in ref. 50. The N_2 binding energy of the **E_3** state is relative to the lowest-energy model **OBS_6-DH_2** (Fig. 2k). The spin states and BS solutions of these five models from **E_0** to **E_4** states are BS147 (M_S = 1/2), BS346 (M_S = 2), BS235 (M_S = 1/2), BS147 (M_S = 0), and BS234 (M_S = 1/2), respectively.

energy (22.6 kcal mol^{-1}). Starting an optimization with N_2 instead *trans* to the Fe2–C bond (Fig. 7c), however, leads to the spontaneous formation of the **OBS_6-2BH_{26}-N_2@Fe2** isomer (see Fig. 7d and Fig. 6). Comparing the **OBS_6-DH_2** isomer instead we find that N_2 binding *cis* to the Fe2–C bond (Fig. 7f) is even more unfavourable (25.6 kcal mol^{-1}) and binding *trans* (Fig. 7g) is still fairly unfavourable compared to the **OBS_6-2BH_{26}** and **OBS_2-2BH_{26}** structures. These results suggest that it is rather bridging hydrides between Fe_2 and Fe_6 that enhance N_2 binding than a H_2 ligand.

Comparing N_2 binding energies across the FeMoco redox series: $\mathbf{E_0}$, $\mathbf{E_1}$, $\mathbf{E_2}$, and $\mathbf{E_4}$ states (using the models discussed in our recent work[50]), the binding energy of N_2 to the $\mathbf{E_3}$ state is found to be marginally more favorable than $\mathbf{E_2}$ and not as favorable as binding to the $\mathbf{E_4}$ state (see Fig. 8), which is similar to trends reported by Ryde and Jiang.[51] The ligand-field diagrams of Fe2 and Fe6 with bound N_2 in Fig. 6 (obtained from diamagnetic substitution and QROs) show that both Fe ions are low-spin Fe^{3+} in an approximate octahedral ligand-field and two d_{xz} and d_{yz} orbitals overlap with π^* orbitals of N_2 (see Fig. S15, ESI†), which is very similar to that found for the $\mathbf{E_4}$ state in our previous study.[50] We previously suggested that a low-spin electronic structure on the Fe site is generally encountered in almost all N_2-bound FeMoco structures, and that such spin-paired electronic structure is likely assisted by the strong sigma-donor hydrides, especially when more favorable hydride ligation is made possible by an open belt sulfide bridge.[50] While the $\mathbf{E_3}$ models **OBS_2-2BH_{26}** and **OBS_6-2BH_{26}** models have the same di-hydride geometric and electronic structure features, the binding energy is predicted to be less than the $\mathbf{E_4}$ state, probably related to an overall less-reduced Fe environment in $\mathbf{E_3}$ that decreases backbonding to the N_2 ligand.

Conclusions

In this study we have discussed the energy surface of the $\mathbf{E_3}$ redox state of FeMoco and attempted to shed light on the possible forms that this complicated cofactor can take upon addition of 3 electrons and 3 protons (relative to the $\mathbf{E_0}$ state). This fills an important gap in the literature in our opinion as so little is known experimentally about this state, being EPR-silent by traditional EPR spectroscopy and hard to isolate. In fact, no spectroscopic data is available on this state and only indirect kinetic data is available.[1,24] Furthermore, only a few computational studies[31,33,51] have been devoted to the state.

Our results suggest that the most likely structure of the $\mathbf{E_3}$-state cofactor involves structures with a protonated S2B sulfide bridge in an open form, *i.e.* a terminal sulfhydryl group on Fe6, which allows a few different Fe–H structures to form (all of them involving 2 hydrides or at least 2 Fe–H interactions). One of these models includes 2 bridging hydrides between Fe2 and Fe6 (Fig. 2g), a structure similar to an $\mathbf{E_4}$ model previously discussed by us and others,[9,32,34] while another model (Fig. 2i) features 1 bridging, 1 terminal hydride instead (similar to the lowest energy $\mathbf{E_4}$ structure in a recent study by us[50]). The third structure is a bit different, instead of featuring individual Fe–hydrides, it takes a form best described as a side-on Fe–(H_2) ligand at the Fe2 site. Energetically, these 3 structures are essentially equivalent when calculated using our QM/MM model with a small QM-region and using the r^2SCAN density functional, being $\sim$1 kcal mol^{-1} of each other, with the Fe–H_2 structure marginally favoured. Upon increasing the QM-region we find a slight shift in relative energies for these 3 isomers, favouring the Fe–H_2 structure, **OBS_6-DH_2** (being $\sim$3 kcal mol^{-1} lower in energy than the other two).

The electronic structures of these 3 states, analyzed *via* localized orbital analysis, show considerable differences as shown in Fig. 5. Structure **OBS_6-DH_2 (k)** in particular, with an Fe–H_2 interaction, features 2 localized electrons associated with the H_2, while structures **OBS_6-2BH_{26} (g)** and **OBS_6-BH_{26}-TH_2 (i)** are more similar and feature 4 electrons associated with the bridging/terminal hydride atoms. Such a distinct difference in electronic structure might be expected to give rise to considerable functional dependency.

The functional dependency on isomer energies is predicted to be fairly mild when evaluated using 3 different functionals that we have previously found to describe the molecular and electronic structures of spin-coupled iron–sulfur clusters well: r^2SCAN, B97-D3, TPSSh. The results of these three functionals show that **OBS_6-2BH_{26} (g)**, **OBS_6-BH_{26}-TH_2 (i)**, and **OBS_6-DH_2 (k)** are the 3 most favourable models. However, the B3LYP* functional (previously found to behave similarly to the other 3 functionals for geometries)[56] interestingly favours a triply protonated carbide.

The functional dependency of FeMoco isomers is actually known to be extremely sensitive in general, especially with respect to Hartree–Fock exchange, as discussed by Ryde and coworkers for energies[110] and Harvey and coworkers for electron density changes.[111] Functionals such as B3LYP and other hybrids with at least 20% HF exchange are *e.g.* known to predict interstitial carbide protonation in both $\mathbf{E_3}$ and $\mathbf{E_4}$ redox states[31,110] and it seems that this also applies to the 15% B3LYP* functional.

However, there is no experimental evidence for carbide protonation occurring in any FeMoco state. In fact, according to recent ^{13}C ENDOR studies of multiple trapped FeMoco states with labelled interstitial carbide,[112] the carbide hyperfine coupling is practically unchanged. A likely interpretation is that the carbide appears more likely to have a general stabilizing role[112] during catalysis. Together with the observation that most hybrid functionals also predict worse FeMoco structures (overestimating Fe–Fe, Fe–S and Fe–C distances) our interpretation is that only non-hybrid functionals and functionals with 0–10% HF exchange describe FeMoco qualitatively correctly.

Uncertainty about the functional dependency nonetheless remains that needs to be evaluated on a case-by-case basis. In recent previous work we compared the energies of **E_2-hyd** and **E_2-nonhyd** isomers that were found to be highly sensitive to the use of r^2SCAN vs TPSSh.[50] That sensitivity could be explained as the two isomers differing in the nature of the localization of added electrons (Fe-reduction *vs.* forming H^-). Jiang and Ryde

have also reported different trends for the $\mathbf{E_2}$ state comparing TPSS, r^{2}SCAN and TPSSh.[37] The nature of the electronic structure of reduced FeMoco isomers hence continues to present challenges to density functional treatments, both in terms of accuracy and interpretation of the complex electronic structure. The electronic structure interpretation of the $\mathbf{E_3}$ isomers discussed in Section E is far from straightforward and as shown in the ESI,† different functionals also give slightly different electronic structures (different BS solutions, different Fe–H covalency and different degrees of localization/delocalization). A systematic assessment of density functionals for the description of Fe–hydride bonds in open-shell Fe compounds is likely to be useful to shed further light on these matters. Overall, our understanding of the electronic structure of hydride-based FeMoco structures remains very much incomplete and continues to surprise us. The flexibility of hydride conformers found in this study is possibly part of a general phenomenon of dynamical flexibility of Fe-bound hydrides as *e.g.* discussed in recent temperature-dependent studies of an $[Fe_2H_2]$ dimer studied by Holland and coworkers.[113]

N_2 binding was explored to $\mathbf{OBS_6\text{-}2BH_{26}}$ isomers and resulted in end-on N_2-bound isomers similar to those studied in recent work.[34,50] Conversely, N_2 binding to $\mathbf{OBS_6\text{-}DH_2}$ and $\mathbf{OBS_6\text{-}BH_{26}\text{-}TH_2}$ isomers was found to be unfavourable. Analysis of the electronic structure of the most favourable N_2-bound state reveals that a low-spin Fe(III) state is found at the N_2-binding Fe ion. However, the binding energy of N_2 relative to the most stable $\mathbf{E_3}$ isomer ($\mathbf{OBS_6\text{-}DH_2}$), is found to be slightly uphill, suggesting that the $\mathbf{E_3}$ redox isomer may not be reduced enough to favourable bind N_2. Considering the overall uncertainty from factors such as QM model size, the lack of thermal contributions, as well as the functional dependency, the calculations suggest isomers $\mathbf{OBS_6\text{-}2BH_{26}}$, $\mathbf{OBS_6\text{-}BH_{26}\text{-}TH_2}$ and $\mathbf{OBS_6\text{-}DH_2}$ as the most favourable and we do not attempt to distinguish between them at this stage. Any of these 3 states may represent species formed under experimental conditions, however, $\mathbf{E_3}$ has never been isolated, so very little is actually known experimentally. Both $\mathbf{E_2}$ and $\mathbf{E_4}$ are known to evolve H_2 if the electron-flux rate is slower than the rate for the H_2 formation, and $\mathbf{E_3}$ is likely to be similar in this respect. This means that the $\mathbf{E_3}$ state would be meta-stable with respect to H_2 formation. The stable $\mathbf{OBS_6\text{-}DH_2}$ isomer found in this study, containing an H_2 ligand, could actually represent a state on the path towards evolving H_2 and falling back to $\mathbf{E_1}$. An isolable $\mathbf{E_3}$ state may then instead be better represented by either $\mathbf{OBS_6\text{-}2BH_{26}}$ or $\mathbf{OBS_6\text{-}BH_{26}\text{-}TH_2}$, depending on the barriers present. Future work will have to consider the calculation of reaction pathways and barriers relating all $\mathbf{E_3}$ species from the initial formation of the state until the H_2 formation.

Author contributions

The manuscript was written through contributions of all authors.

Conflicts of interest

There are no conflicts to declare.

Acknowledgements

R. B. acknowledges support from the Max Planck society. Y. P. acknowledges a scholarship from the China Scholarship Council and a grant from the National Natural Science Foundation of China (no. 22073010). Open Access funding provided by the Max Planck Society.

References

1 B. K. Burgess and D. J. Lowe, Mechanism of Molybdenum Nitrogenase, *Chem. Rev.*, 1996, **96**, 2983–3012.
2 O. Einsle and D. C. Rees, Structural Enzymology of Nitrogenase Enzymes, *Chem. Rev.*, 2020, **120**, 4969–5004.
3 A. J. Jasniewski, C. C. Lee, M. W. Ribbe and Y. Hu, Reactivity, Mechanism, and Assembly of the Alternative Nitrogenases, *Chem. Rev.*, 2020, **120**, 5107–5157.
4 H. L. Rutledge and F. A. Tezcan, Electron Transfer in Nitrogenase, *Chem. Rev.*, 2020, **120**, 5158–5193.
5 L. C. Seefeldt, Z. Y. Yang, D. A. Lukoyanov, D. F. Harris, D. R. Dean, S. Raugei and B. M. Hoffman, Reduction of Substrates by Nitrogenases, *Chem. Rev.*, 2020, **120**, 5082–5106.
6 C. Van Stappen, L. Decamps, G. E. Cutsail, R. Bjornsson, J. T. Henthorn, J. A. Birrell and S. DeBeer, The Spectroscopy of Nitrogenases, *Chem. Rev.*, 2020, **120**, 5005–5081.
7 Z. Y. Yang, N. Khadka, D. Lukoyanov, B. M. Hoffman, D. R. Dean and L. C. Seefeldt, On reversible H2 loss upon N2 binding to FeMo-cofactor of nitrogenase, *Proc. Natl. Acad. Sci. U. S. A.*, 2013, **110**, 16327–16332.
8 D. Lukoyanov, N. Khadka, Z. Y. Yang, D. R. Dean, L. C. Seefeldt and B. M. Hoffman, Reductive Elimination of H2 Activates Nitrogenase to Reduce the N identical withN Triple Bond: Characterization of the E4(4H) Janus Intermediate in Wild-Type Enzyme, *J. Am. Chem. Soc.*, 2016, **138**, 10674–10683.
9 V. Hoeke, L. Tociu, D. A. Case, L. C. Seefeldt, S. Raugei and B. M. Hoffman, High-Resolution ENDOR Spectroscopy Combined with Quantum Chemical Calculations Reveals the Structure of Nitrogenase Janus Intermediate E4(4H), *J. Am. Chem. Soc.*, 2019, **141**, 11984–11996.
10 E. Münck, H. Rhodes, W. H. Orme-Johnson, L. C. Davis, W. J. Brill and V. K. Shah, Nitrogenase. VIII. Mössbauer and EPR spectroscopy. The MoFe protein component from Azotobacter vinelandii OP, *Biochim. Biophys. Acta, Protein Struct.*, 1975, **400**, 32–53.
11 J. Rawlings, V. K. Shah, J. R. Chisnell, W. J. Brill, R. Zimmermann, E. Münck and W. H. Orme-Johnson, Novel metal cluster in the iron-molybdenum cofactor of nitrogenase. Spectroscopic evidence, *J. Biol. Chem.*, 1978, **253**, 1001–1004.

12 T. V. Morgan, L. E. Mortenson, J. W. McDonald and G. D. Watt, Comparison of redox and EPR properties of the molybdenum iron proteins of Clostridium pasteurianum and Azotobacter vinelandii nitrogenases, *J. Inorg. Biochem.*, 1988, **33**, 111–120.

13 K. Fisher, W. E. Newton and D. J. Lowe, Electron Paramagnetic Resonance Analysis of Different Azotobacter vinelandii Nitrogenase MoFe-Protein Conformations Generated during Enzyme Turnover: Evidence for S = 3/2 Spin States from Reduced MoFe-Protein Intermediates, *Biochemistry*, 2001, **40**, 3333–3339.

14 O. Einsle, F. A. Tezcan, S. L. A. Andrade, B. Schmid, M. Yoshida, J. B. Howard and D. C. Rees, Nitrogenase MoFe-Protein at 1.16 Å Resolution: A Central Ligand in the FeMo-Cofactor, *Science*, 2002, **297**, 1696–1700.

15 T. Spatzal, M. Aksoyoglu, L. Zhang, S. L. Andrade, E. Schleicher, S. Weber, D. C. Rees and O. Einsle, Evidence for interstitial carbon in nitrogenase FeMo cofactor, *Science*, 2011, **334**, 940.

16 S. J. Yoo, H. C. Angove, V. Papaefthymiou, B. K. Burgess and E. Münck, Mössbauer Study of the MoFe Protein of Nitrogenase from Azotobacter vinelandii Using Selective 57Fe Enrichment of the M-Centers, *J. Am. Chem. Soc.*, 2000, **122**, 4926–4936.

17 C. Van Stappen, R. Davydov, Z. Y. Yang, R. Fan, Y. Guo, E. Bill, L. C. Seefeldt, B. M. Hoffman and S. DeBeer, Spectroscopic Description of the E1 State of Mo Nitrogenase Based on Mo and Fe X-ray Absorption and Mössbauer Studies, *Inorg. Chem.*, 2019, **58**, 12365–12376.

18 C. Van Stappen, A. T. Thorhallsson, L. Decamps, R. Bjornsson and S. DeBeer, Resolving the structure of the E1 state of Mo nitrogenase through Mo and Fe K-edge EXAFS and QM/MM calculations, *Chem. Sci.*, 2019, **10**, 9807–9821.

19 D. Lukoyanov, B. M. Barney, D. R. Dean, L. C. Seefeldt and B. M. Hoffman, Connecting nitrogenase intermediates with the kinetic scheme for N2 reduction by a relaxation protocol and identification of the N2 binding state, *Proc. Natl. Acad. Sci. U. S. A.*, 2007, **104**, 1451–1455.

20 D. Lukoyanov, Z. Y. Yang, S. Duval, K. Danyal, D. R. Dean, L. C. Seefeldt and B. M. Hoffman, A confirmation of the quench-cryoannealing relaxation protocol for identifying reduction states of freeze-trapped nitrogenase intermediates, *Inorg. Chem.*, 2014, **53**, 3688–3693.

21 D. A. Lukoyanov, N. Khadka, Z. Y. Yang, D. R. Dean, L. C. Seefeldt and B. M. Hoffman, Hydride Conformers of the Nitrogenase FeMo-cofactor Two-Electron Reduced State E2(2H), Assigned Using Cryogenic Intra Electron Paramagnetic Resonance Cavity Photolysis, *Inorg. Chem.*, 2018, **57**, 6847–6852.

22 D. F. Harris, A. Badalyan and L. C. Seefeldt, Mechanistic Insights into Nitrogenase FeMo-Cofactor Catalysis through a Steady-State Kinetic Model, *Biochemistry*, 2022, **61**, 2131–2137.

23 R. Y. Igarashi, M. Laryukhin, P. C. Dos Santos, H.-I. Lee, D. R. Dean, L. C. Seefeldt and B. M. Hoffman, Trapping H- Bound to the Nitrogenase FeMo-Cofactor Active Site during H2 Evolution: Characterization by ENDOR Spectroscopy, *J. Am. Chem. Soc.*, 2005, **127**, 6231–6241.

24 R. N. F. Thorneley and D. J. Lowe, in *Molybdenum Enzymes*, ed. T. G. Spiro, Wiley, New York, 1985, pp. 221–284.

25 D. J. Lowe, K. Fisher and R. N. F. Thorneley, Klebsiella pneumoniae nitrogenase. Mechanism of acetylene reduction and its inhibition by carbon monoxide, *Biochem. J.*, 1990, **272**, 621–625.

26 K. Fisher, M. J. Dilworth and W. E. Newton, Differential Effects on N2 Binding and Reduction, HD Formation, and Azide Reduction with α-195His- and α-191Gln-Substituted MoFe Proteins of Azotobacter vinelandii Nitrogenase, *Biochemistry*, 2000, **39**, 15570–15577.

27 K. M. Lancaster, M. Roemelt, P. Ettenhuber, Y. Hu, M. W. Ribbe, F. Neese, U. Bergmann and S. DeBeer, X-ray Emission Spectroscopy Evidences a Central Carbon in the Nitrogenase Iron-Molybdenum Cofactor, *Science*, 2011, **334**, 974–977.

28 R. Bjornsson, F. A. Lima, T. Spatzal, T. Weyhermüller, P. Glatzel, E. Bill, O. Einsle, F. Neese and S. DeBeer, Identification of a spin-coupled Mo(iii) in the nitrogenase iron–molybdenum cofactor, *Chem. Sci.*, 2014, **5**, 3096–3103.

29 T. Spatzal, J. Schlesier, E. M. Burger, D. Sippel, L. Zhang, S. L. Andrade, D. C. Rees and O. Einsle, Nitrogenase FeMoco investigated by spatially resolved anomalous dispersion refinement, *Nat. Commun.*, 2016, **7**, 10902.

30 R. Bjornsson, F. Neese and S. DeBeer, Revisiting the Mössbauer Isomer Shifts of the FeMoco Cluster of Nitrogenase and the Cofactor Charge, *Inorg. Chem.*, 2017, **56**, 1470–1477.

31 L. Cao, O. Caldararu and U. Ryde, Protonation and Reduction of the FeMo Cluster in Nitrogenase Studied by Quantum Mechanics/Molecular Mechanics(QM/MM) Calculations, *J. Chem. Theory Comput.*, 2018, **14**, 6653–6678.

32 S. Raugei, L. C. Seefeldt and B. M. Hoffman, Critical computational analysis illuminates the reductive-elimination mechanism that activates nitrogenase for N2 reduction, *Proc. Natl. Acad. Sci. U. S. A.*, 2018, **115**, E10521–E10530.

33 I. Dance, Survey of the Geometric and Electronic Structures of the Key Hydrogenated Forms of FeMo-co, the Active Site of the Enzyme Nitrogenase: Principles of the Mechanistically Significant Coordination Chemistry, *Inorganics*, 2019, **7**, 8.

34 A. T. Thorhallsson, B. Benediktsson and R. Bjornsson, A model for dinitrogen binding in the E4 state of nitrogenase, *Chem. Sci.*, 2019, **10**, 11110–11124.

35 L. Cao and U. Ryde, What Is the Structure of the E4 Intermediate in Nitrogenase?, *J. Chem. Theory Comput.*, 2020, **16**, 1936–1952.

36 A. T. Thorhallsson and R. Bjornsson, The E2 state of FeMoco: Hydride Formation versus Fe Reduction and a Mechanism for H2 Evolution, *Chem. – Eur. J.*, 2021, **27**, 16788–16800.

37 H. Jiang, O. K. G. Svensson and U. Ryde, QM/MM Study of Partial Dissociation of S2B for the E(2) Intermediate of Nitrogenase, *Inorg. Chem.*, 2022, **61**, 18067–18076.
38 I. Dance, How feasible is the reversible S-dissociation mechanism for the activation of FeMo-co, the catalytic site of nitrogenase?, *Dalton Trans.*, 2019, **48**, 1251–1262.
39 P. E. M. Siegbahn, The mechanism for nitrogenase including all steps, *Phys. Chem. Chem. Phys.*, 2019, **21**, 15747–15759.
40 L. Cao and U. Ryde, N2H2 binding to the nitrogenase FeMo cluster studied by QM/MM methods, *J. Biol. Inorg. Chem.*, 2020, **25**, 521–540.
41 L. Cao and U. Ryde, Putative reaction mechanism of nitrogenase after dissociation of a sulfide ligand, *J. Catal.*, 2020, **391**, 247–259.
42 I. Dance, Computational Investigations of the Chemical Mechanism of the Enzyme Nitrogenase, *ChemBioChem*, 2020, **21**, 1671–1709.
43 I. Dance, Structures and reaction dynamics of N2 and H2 binding at FeMo-co, the active site of nitrogenase, *Dalton Trans.*, 2021, **50**, 18212–18237.
44 I. Dance, Calculating the chemical mechanism of nitrogenase: new working hypotheses, *Dalton Trans.*, 2022, **51**, 12717–12728.
45 I. Dance, Understanding the tethered unhooking and rehooking of S2B in the reaction domain of FeMo-co, the active site of nitrogenase, *Dalton Trans.*, 2022, **51**, 15538–15554.
46 H. Jiang and U. Ryde, Thermodynamically Favourable States in the Reaction of Nitrogenase without Dissociation of any Sulfide Ligand, *Chemistry*, 2022, e202103933.
47 H. Jiang, O. K. G. Svensson, L. Cao and U. Ryde, Proton Transfer Pathways in Nitrogenase with and without Dissociated S2B, *Angew. Chem., Int. Ed.*, 2022, **61**, e202208544.
48 W. J. Wei and P. E. M. Siegbahn, A Mechanism for Nitrogenase Including Loss of a Sulfide, *Chemistry*, 2022, **28**, e202103745.
49 I. Dance, The binding of reducible N(2) in the reaction domain of nitrogenase, *Dalton Trans.*, 2023, **52**, 2013–2026.
50 Y. Pang and R. Bjornsson, Understanding the Electronic Structure Basis for N2 Binding to FeMoco: A Systematic Quantum Mechanics/Molecular Mechanics Investigation, *Inorg. Chem.*, 2023, **62**, 5357–5375.
51 H. Jiang and U. Ryde, N(2) binding to the E(0)-E(4) states of nitrogenase, *Dalton Trans.*, 2023, **52**, 9104–9120.
52 B. Benediktsson and R. Bjornsson, QM/MM Study of the Nitrogenase MoFe Protein Resting State: Broken-Symmetry States, Protonation States, and QM Region Convergence in the FeMoco Active Site, *Inorg. Chem.*, 2017, **56**, 13417–13429.
53 B. Benediktsson, A. T. Thorhallsson and R. Bjornsson, QM/MM calculations reveal a bridging hydroxo group in a vanadium nitrogenase crystal structure, *Chem. Commun.*, 2018, **54**, 7310–7313.
54 B. Benediktsson and R. Bjornsson, Quantum Mechanics/Molecular Mechanics Study of Resting-State Vanadium Nitrogenase: Molecular and Electronic Structure of the Iron-Vanadium Cofactor, *Inorg. Chem.*, 2020, **59**, 11514–11527.
55 N. Spiller, R. Bjornsson, S. DeBeer and F. Neese, Carbon Monoxide Binding to the Iron-Molybdenum Cofactor of Nitrogenase: a Detailed Quantum Mechanics/Molecular Mechanics Investigation, *Inorg. Chem.*, 2021, **60**, 18031–18047.
56 B. Benediktsson and R. Bjornsson, Analysis of the Geometric and Electronic Structure of Spin-Coupled Iron-Sulfur Dimers with Broken-Symmetry DFT: Implications for FeMoco, *J. Chem. Theory Comput.*, 2022, **18**, 1437–1457.
57 T. V. Harris and R. K. Szilagyi, Comparative Assessment of the Composition and Charge State of Nitrogenase FeMo-Cofactor, *Inorg. Chem.*, 2011, **50**, 4811–4824.
58 L. Cao, O. Caldararu and U. Ryde, Protonation States of Homocitrate and Nearby Residues in Nitrogenase Studied by Computational Methods and Quantum Refinement, *J. Phys. Chem. B*, 2017, **121**, 8242–8262.
59 T. Lovell, J. Li, T. Liu, D. A. Case and L. Noodleman, FeMo Cofactor of Nitrogenase: A Density Functional Study of States MN, MOX, MR, and MI, *J. Am. Chem. Soc.*, 2001, **123**, 12392–12410.
60 T. Lovell, R. A. Torres, W.-G. Han, T. Liu, D. A. Case and L. Noodleman, Metal Substitution in the Active Site of Nitrogenase MFe7S9 (M = Mo^{4+}, V^{3+}, Fe^{3+}), *Inorg. Chem.*, 2002, **41**, 5744–5753.
61 ASH - a multiscale modelling program, Version 0.9; Ragnar Bjornsson, 2022.
62 P. Eastman, J. Swails, J. D. Chodera, R. T. McGibbon, Y. Zhao, K. A. Beauchamp, L. P. Wang, A. C. Simmonett, M. P. Harrigan, C. D. Stern, R. P. Wiewiora, B. R. Brooks and V. S. Pande, OpenMM 7: Rapid development of high performance algorithms for molecular dynamics, *PLoS Comput. Biol.*, 2017, **13**, e1005659.
63 F. Neese, F. Wennmohs, U. Becker and C. Riplinger, The ORCA quantum chemistry program package, *J. Chem. Phys.*, 2020, **152**, 224108.
64 R. B. Best, X. Zhu, J. Shim, P. E. Lopes, J. Mittal, M. Feig and A. D. Mackerell, Optimization of the additive CHARMM all-atom protein force field targeting improved sampling of the backbone phi, psi and side-chain chi(1) and chi(2) dihedral angles, *J. Chem. Theory Comput.*, 2012, **8**, 3257–3273.
65 P. Sherwood, A. H. de Vries, M. F. Guest, G. Schreckenbach, C. R. A. Catlow, S. A. French, A. A. Sokol, S. T. Bromley, W. Thiel, A. J. Turner, S. Billeter, F. Terstegen, S. Thiel, J. Kendrick, S. C. Rogers, J. Casci, M. Watson, F. King, E. Karlsen, M. Sjøvoll, A. Fahmi, A. Schäfer and C. Lennartz, QUASI: A general purpose implementation of the QM/MM approach and its application to problems in catalysis, *J. Mol. Struct. THEOCHEM*, 2003, **632**, 1–28.
66 L.-P. Wang and C. Song, Geometry optimization made simple with translation and rotation coordinates, *J. Chem. Phys.*, 2016, **144**, 214108.
67 S. R. Billeter, A. J. Turner and W. Thiel, Linear scaling geometry optimisation and transition state search in

hybrid delocalised internal coordinates, *Phys. Chem. Chem. Phys.*, 2000, **2**, 2177–2186.
68 J. W. Furness, A. D. Kaplan, J. Ning, J. P. Perdew and J. Sun, Accurate and Numerically Efficient r(2)SCAN Meta-Generalized Gradient Approximation, *J. Phys. Chem. Lett.*, 2020, **11**, 8208–8215.
69 J. Tao, J. P. Perdew, V. N. Staroverov and G. E. Scuseria, Climbing the Density Functional Ladder: Nonempirical Meta--Generalized Gradient Approximation Designed for Molecules and Solids, *Phys. Rev. Lett.*, 2003, **91**, 146401.
70 Y. Zhao and D. G. Truhlar, A new local density functional for main-group thermochemistry, transition metal bonding, thermochemical kinetics, and noncovalent interactions, *J. Chem. Phys.*, 2006, **125**, 194101.
71 S. Grimme, Semiempirical GGA-type density functional constructed with a long-range dispersion correction, *J. Comput. Chem.*, 2006, **27**, 1787–1799.
72 S. Grimme, J. Antony, S. Ehrlich and H. Krieg, A consistent and accurate ab initio parametrization of density functional dispersion correction (DFT-D) for the 94 elements H-Pu, *J. Chem. Phys.*, 2010, **132**, 154104.
73 S. Grimme, S. Ehrlich and L. Goerigk, Effect of the damping function in dispersion corrected density functional theory, *J. Comput. Chem.*, 2011, **32**, 1456–1465.
74 M. Reiher, O. Salomon and B. Artur Hess, Reparameterization of hybrid functionals based on energy differences of states of different multiplicity, *Theor. Chem. Acc.*, 2001, **107**, 48–55.
75 O. Salomon, M. Reiher and B. A. Hess, Assertion and validation of the performance of the B3LYP functional for the first transition metal row and the G2 test set, *J. Chem. Phys.*, 2002, **117**, 4729–4737.
76 A. D. Becke, Density-functional exchange-energy approximation with correct asymptotic behavior, *Phys. Rev. A: At., Mol., Opt. Phys.*, 1988, **38**, 3098–3100.
77 C. Lee, W. Yang and R. G. Parr, Development of the Colle-Salvetti correlation-energy formula into a functional of the electron density, *Phys. Rev. B: Condens. Matter Mater. Phys.*, 1988, **37**, 785–789.
78 A. D. Becke, Density-functional thermochemistry. III. The role of exact exchange, *J. Chem. Phys.*, 1993, **98**, 5648–5652.
79 C. van Wüllen, Molecular density functional calculations in the regular relativistic approximation: Method, application to coinage metal diatomics, hydrides, fluorides and chlorides, and comparison with first-order relativistic calculations, *J. Chem. Phys.*, 1998, **109**, 392–399.
80 E. Caldeweyher, C. Bannwarth and S. Grimme, Extension of the D3 dispersion coefficient model, *J. Chem. Phys.*, 2017, **147**, 034112.
81 S. Ehlert, U. Huniar, J. Ning, J. W. Furness, J. Sun, A. D. Kaplan, J. P. Perdew and J. G. Brandenburg, r(2)SCAN-D4: Dispersion corrected meta-generalized gradient approximation for general chemical applications, *J. Chem. Phys.*, 2021, **154**, 061101.
82 F. Neese, An improvement of the resolution of the identity approximation for the formation of the Coulomb matrix, *J. Comput. Chem.*, 2003, **24**, 1740–1747.
83 F. Weigend and R. Ahlrichs, Balanced basis sets of split valence, triple zeta valence and quadruple zeta valence quality for H to Rn: Design and assessment of accuracy, *Phys. Chem. Chem. Phys.*, 2005, **7**, 3297–3305.
84 D. A. Pantazis and F. Neese, All-electron scalar relativistic basis sets for the 6p elements, *Theor. Chem. Acc.*, 2012, 131.
85 D. A. Pantazis, X.-Y. Chen, C. R. Landis and F. Neese, All-Electron Scalar Relativistic Basis Sets for Third-Row Transition Metal Atoms, *J. Chem. Theory Comput.*, 2008, **4**, 908–919.
86 J. D. Rolfes, F. Neese and D. A. Pantazis, All-electron scalar relativistic basis sets for the elements Rb-Xe, *J. Comput. Chem.*, 2020, **41**, 1842–1849.
87 F. L. Hirshfeld, Bonded-atom fragments for describing molecular charge densities, *Theor. Chem. Acc.*, 1977, **44**, 129–138.
88 R. S. Mulliken, Electronic Population Analysis on LCAO–MO Molecular Wave Functions. I, *J. Chem. Phys.*, 1955, **23**, 1833–1840.
89 H. Li and J. H. Jensen, Partial Hessian vibrational analysis: the localization of the molecular vibrational energy and entropy, *Theor. Chem. Acc.*, 2002, **107**, 211–219.
90 J. Pipek and P. G. Mezey, A fast intrinsic localization procedure applicable for ab initio and semiempirical linear combination of atomic orbital wave functions, *J. Chem. Phys.*, 1989, **90**, 4916–4926.
91 L. C. Seefeldt, B. M. Hoffman and D. R. Dean, Electron transfer in nitrogenase catalysis, *Curr. Opin. Chem. Biol.*, 2012, **16**, 19–25.
92 B. M. Hoffman, D. Lukoyanov, D. R. Dean and L. C. Seefeldt, Nitrogenase: A Draft Mechanism, *Acc. Chem. Res.*, 2013, **46**, 587–595.
93 I. Dance, Misconception of reductive elimination of H2, in the context of the mechanism of nitrogenase, *Dalton Trans.*, 2015, **44**, 9027–9037.
94 P. E. Siegbahn, Model Calculations Suggest that the Central Carbon in the FeMo-Cofactor of Nitrogenase Becomes Protonated in the Process of Nitrogen Fixation, *J. Am. Chem. Soc.*, 2016, **138**, 10485–10495.
95 I. Dance, New insights into the reaction capabilities of His(195) adjacent to the active site of nitrogenase, *J. Inorg. Biochem.*, 2017, **169**, 32–43.
96 L. Cao and U. Ryde, Influence of the protein and DFT method on the broken-symmetry and spin states in nitrogenase, *Int. J. Quantum Chem.*, 2018, **118**, e25627.
97 I. Dance, What is the role of the isolated small water pool near FeMo-co, the active site of nitrogenase?, *FEBS J.*, 2018, **285**, 2972–2986.
98 P. E. M. Siegbahn, Is there computational support for an unprotonated carbon in the E(4) state of nitrogenase?, *J. Comput. Chem.*, 2018, **39**, 743–747.
99 W. J. Wei and P. E. M. Siegbahn, The active E4 structure of nitrogenase studied with different DFT functionals, *J. Comput. Chem.*, 2021, **42**, 81–85.
100 B. M. Barney, R. Y. Igarashi, P. C. Dos Santos, D. R. Dean and L. C. Seefeldt, Substrate interaction at an iron-sulfur

face of the FeMo-cofactor during nitrogenase catalysis, *J. Biol. Chem.*, 2004, **279**, 53621–53624.

101 R. Sarma, B. M. Barney, S. Keable, D. R. Dean, L. C. Seefeldt and J. W. Peters, Insights into substrate binding at FeMo-cofactor in nitrogenase from the structure of an alpha-70(Ile) MoFe protein variant, *J. Inorg. Biochem.*, 2010, **104**, 385–389.

102 T. Spatzal, K. A. Perez, O. Einsle, J. B. Howard and D. C. Rees, Ligand binding to the FeMo-cofactor: Structures of CO-bound and reactivated nitrogenase, *Science*, 2014, **345**, 1620.

103 D. Sippel, M. Rohde, J. Netzer, C. Trncik, J. Gies, K. Grunau, I. Djurdjevic, L. Decamps, S. L. A. Andrade and O. Einsle, A bound reaction intermediate sheds light on the mechanism of nitrogenase, *Science*, 2018, **359**, 1484.

104 W. Kang, C. Lee Chi, J. Jasniewski Andrew, W. Ribbe Markus and Y. Hu, Structural evidence for a dynamic metallocofactor during N2 reduction by Mo-nitrogenase, *Science*, 2020, **368**, 1381–1385.

105 K. L. Skubi and P. L. Holland, So Close, yet Sulfur Away: Opening the Nitrogenase Cofactor Structure Creates a Binding Site, *Biochemistry*, 2018, **57**, 3540–3541.

106 T. M. Buscagan and D. C. Rees, Rethinking the Nitrogenase Mechanism: Activating the Active Site, *Joule*, 2019, **3**, 2662–2678.

107 J. W. Peters, O. Einsle, D. R. Dean, S. DeBeer, B. M. Hoffman, P. L. Holland and L. C. Seefeldt, Comment on Structural evidence for a dynamic metallocofactor during N2 reduction by Mo-nitrogenase, *Science*, 2021, **371**, eabe5481.

108 W. Kang, C. C. Lee, A. J. Jasniewski, M. W. Ribbe and Y. Hu, Response to Comment on Structural evidence for a dynamic metallocofactor during N2 reduction by Mo-nitrogenase, *Science*, 2021, **371**, eabe5856.

109 J. Bergmann, E. Oksanen and U. Ryde, Critical evaluation of a crystal structure of nitrogenase with bound N2 ligands, *J. Biol. Inorg. Chem.*, 2021, **26**, 341–353.

110 L. Cao and U. Ryde, Extremely large differences in DFT energies for nitrogenase models, *Phys. Chem. Chem. Phys.*, 2019, **21**, 2480–2488.

111 C. Martin-Fernandez and J. N. Harvey, On the Use of Normalized Metrics for Density Sensitivity Analysis in DFT, *J. Phys. Chem. A*, 2021, **125**, 4639–4652.

112 D. A. Lukoyanov, Z. Y. Yang, A. Perez-Gonzalez, S. Raugei, D. R. Dean, L. C. Seefeldt and B. M. Hoffman, 13)C ENDOR Characterization of the Central Carbon within the Nitrogenase Catalytic Cofactor Indicates That the CFe6 Core Is a Stabilizing ''Heart of Steel'', *J. Am. Chem. Soc.*, 2022, **144**, 18315–18328.

113 S. F. McWilliams, B. Q. Mercado, K. C. MacLeod, M. S. Fataftah, M. Tarrago, X. Wang, E. Bill, S. Ye and P. L. Holland, Dynamic effects on ligand field from rapid hydride motion in an iron(ii) dimer with an $S = 3$ ground state, *Chem. Sci.*, 2023, **14**, 2303–2312.

